NEUROSCIENCE

Targeting histone K4 trimethylation for treatment of cognitive and synaptic deficits in mouse models of Alzheimer's disease

Qing Cao, Wei Wang, Jamal B. Williams, Fengwei Yang, Zi-Jun Wang, Zhen Yan*

Epigenetic aberration is implicated in aging and neurodegeneration. Using postmortem tissues from patients with Alzheimer's disease (AD) and AD mouse models, we have found that the permissive histone mark H3K4me3 and its catalyzing enzymes are significantly elevated in the prefrontal cortex (PFC). Inhibiting H3K4-specific methyltransferases with the compound WDR5-0103 leads to the substantial recovery of PFC synaptic function and memory-related behaviors in AD mice. Among the up-regulated genes reversed by WDR5-0103 treatment in PFC of AD mice, many have the increased H3K4me3 enrichment at their promoters. One of the identified top-ranking target genes, *Sgk1*, which encodes serum and glucocorticoid-regulated kinase 1, is also significantly elevated in PFC of patients with AD. Administration of a specific Sgk1 inhibitor reduces hyperphosphorylated tau protein, restores PFC glutamatergic synaptic function, and ameliorates memory deficits in AD mice. These results have found a novel epigenetic mechanism and a potential therapeutic strategy for AD and related neurodegenerative disorders.

INTRODUCTION

Neurodegenerative disorders including Alzheimer's disease (AD) and frontotemporal dementia (FTD) are afflicting a large number of people. Mutations in the microtubule-associated protein Tau have been implicated in the pathogenesis of AD and FTD, because of the link of tau tangles to microtubule disassembly, transport impairment, synaptic dysfunction, and neuronal degeneration (*1*–*3*). Effective treatment for these diseases is still lacking, calling for the need to find new strategies to probe the underpinnings of neurodegenerative disorders. Recent evidence suggests that the epigenetic dysregulation, which can lead to alterations of gene expression in brain cognitive regions, is one of the key pathophysiological bases of aging and neurodegeneration (*4*, *5*). Restoring epigenetic homeostasis is considered a promising therapeutic strategy for AD and related disorders (*6*, *7*).

One major mechanism of epigenetic regulation of gene expression is histone modifications and chromatin remodeling. Specific histone modifications are catalyzed in a reversible manner by enzymes with opposing functions, such as histone acetyltransferases/deacetylases and histone methyltransferases (HMTs)/demethylases. Methylation at lysines in histone H3 can serve to both activate and repress gene transcription. Histone methylation is uniquely suitable to be part of the molecular underpinnings of memory storage because of its tight association with distinct transcriptional states of genes and its active regulation during memory processes (*8*, *9*). Consistently, genetic studies have revealed the prominent link of mutations in H3K4 methyltransferases or demethylases to diseases with cognitive impairment (*10*), including Wiedemann-Steiner syndrome (*KMT2A* mutations) (*11*), Kabuki syndrome (*KMT2D* mutations) (*12*), X-linked Claes-Jensen syndrome (*KDM5C* mutations) (*13*), and autism spectrum disorders (*KDM5A/5B* mutations) (*14*).

Our recent studies have found that H3K4 trimethylation (H3K4me3), a histone mark for gene activation (*15*), is significantly elevated in human AD postmortem tissues and AD mouse models in prefrontal cortex (PFC), a command center for high-level "executive" functions including working memory and decision-making (*16*) and a key brain region impaired in AD and FTD (*17*–*19*). We have found that inhibiting H3K4-specific methyltransferases leads to the substantial recovery of glutamatergic synaptic function in PFC pyramidal neurons and the significant improvement of memory-related behaviors in mutant Tau transgenic mice. These results have revealed a novel role of histone methylation in AD pathophysiology and a potential therapeutic strategy for AD and related neurodegenerative disorders associated with tauopathies.

Department of Physiology and Biophysics, School of Medicine and Biomedical Sciences, State University of New York at Buffalo, Buffalo, NY, USA.
*Corresponding author. Email: zhenyan@buffalo.edu

RESULTS

Histone H3K4me3 and its catalyzing enzymes are significantly elevated in PFC of patients with AD and mutant Tau transgenic mice

To elucidate the role of histone methylation in AD, we examined the alterations of histone methylation marks associated with gene activation or silencing in the postmortem PFC (Brodmann's area 10) tissues from patients with AD (five to six Braak stages). Compared with age- or sex-matched control subjects, the level of permissive H3K4me3 in the nuclear fraction of PFC lysates from patients with AD was significantly increased [Fig. 1A; Ctrl: $n = 9$, AD: $n = 11$, $t_{(18)} = 5.4$, $P < 0.001$; t test], while no significant changes were found on the level of repressive H3K27me3 or enhancer H3K4me. Immunostaining of H3K4me3 and NeuN showed that fluorescent signal intensity of prefrontal cortical neurons immunostained with H3K4me3 in patients with AD were significantly elevated [Fig. 1B; $n = 10$ to 12 slices from three humans per group; $t_{(20)} = 5.9$, $P < 0.001$; t test].

To find out whether aberrant histone methylation also occurs in mouse models of AD, we examined P301S transgenic Tau mice (PS19), a model of tauopathy associated with neurodegenerative diseases including AD and FTD (*20*–*23*). As shown in Fig. 1C, P301S transgenic Tau mice (5 to 6 months old) exhibited a significantly increased level of nuclear H3K4me3 in the PFC, compared to wild-type (WT) mice [WT: $n = 5$, Tau: $n = 6$, $t_{(9)} = 3.8$, $P < 0.01$; t test], while the level of nuclear H3K27me3 and H3K4me had little changes, consistent with the postmortem AD human results.

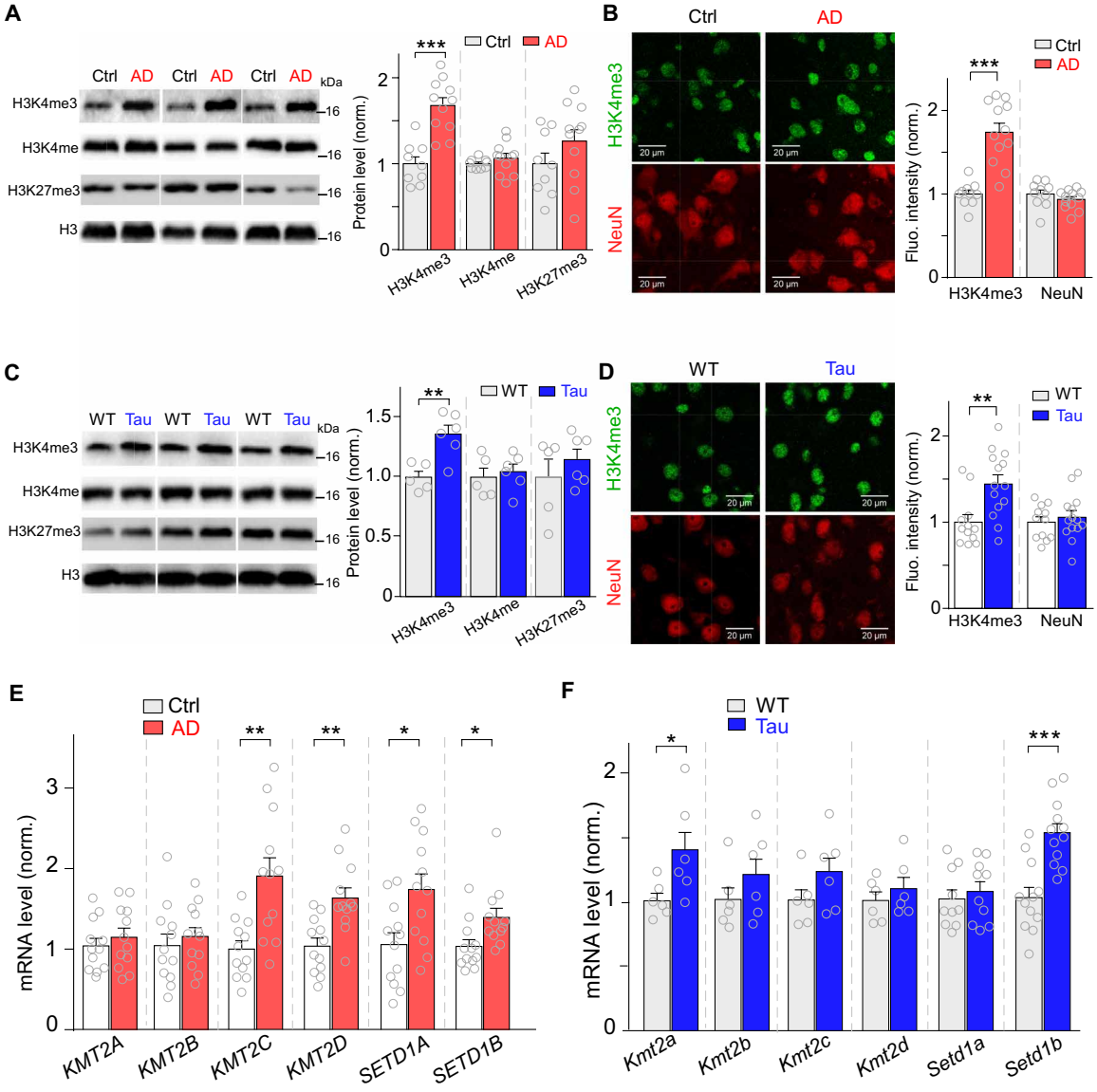

Fig. 1. The level of H3K4me3 and its catalyzing enzymes SET1/MLL HMTs are significantly elevated in the PFC of postmortem tissue from patients with AD and P301S Tau mice. (**A**) Immunoblots and quantification analysis of H3K4me3, H3K4me, and H3K27me3 in the nuclear fraction of postmortem prefrontal cortical tissue (Brodmann's area 10) from patients with AD versus age- and sex-matched control (ctrl) subjects. (**B**) Confocal images and quantification of the intensity of H3K4me3 and NeuN signals of PFC neurons immunostained with H3K4me3 and NeuN in AD and control subjects. (**C**) Immunoblots and quantification analysis of H3K4me3, H3K4me, and H3K27me3 in the nuclear fraction of PFC from P301S transgenic Tau mice (Tau; 5 to 6 months old) versus wild-type (WT) mice. (**D**) Confocal images and quantification of the intensity of H3K4me3 and NeuN signals of PFC neurons immunostained with H3K4me3 and NeuN in WT versus P301S Tau mice. (**E** and **F**) Quantitative polymerase chain reaction (qPCR) data showing the mRNA level of SET1/MLL family members KMT2A-D and SETD1A/B in PFC of postmortem tissue from patients with AD versus control subjects (E) and P301S Tau mice (5 to 6 months old) versus age-matched WT mice (F). In all figures, *$P < 0.05$, **$P < 0.01$, and ***$P < 0.001$, *t* test.

Immunostaining of H3K4me3 and NeuN also confirmed that H3K4me3 signals in PFC neurons of P301S Tau mice were significantly elevated [Fig. 1D; $n = 12$ to 14 slices from four to six mice per group; $t_{(24)} = 3.1$, $P < 0.01$; *t* test]. In the hippocampus of P301S Tau mice, the level of nuclear H3K4me3 did not show significant changes (fig. S1). These findings suggest that the specific elevation of permissive H3K4me3 in PFC of AD could provide a potential mechanism for the activation of genes involved in AD pathophysiology.

Next, we sought to investigate the potential basis for the observed increase of H3K4me3 in patients with AD and P301S Tau mice. We examined the expression of SET1/MLL family of HMTs that are responsible for H3K4me3, including SETD1a/b and MLL1-4 (also named as KMT2A-D) (*24*). As shown in Fig. 1 (E and F), the mRNA level of *KMT2C*, *KMT2D*, *SETD1A*, and *SETD1B* was significantly elevated in patients with AD, compared to control subjects [Ctrl: $n = 12$, AD: $n = 12$, *KMT2C*, $t_{(22)} = 3.6$, $P < 0.01$; *KMT2D*, $t_{(22)} = 3.7$, $P < 0.01$; *SETD1A*, $t_{(22)} = 2.8$, $P < 0.05$; *SETD1B*, $t_{(22)} = 2.6$, $P < 0.05$; *t* test]. In P301S Tau mice, *Kmt2a and Setd1b* were significantly higher, compared to WT mice [$n = 6$ to 12 mice per group; *Kmt2a*, $t_{(10)} = 2.4$, $P < 0.05$; *Setd1b*, $t_{(22)} = 4.7$, $P < 0.001$; *t* test], while others were not significantly altered. These results reveal the up-regulation of SET1/MLL family of HMTs as a potential

cause for the aberrantly high H3K4me3 in patients with AD and P301S Tau mice.

Treatment with the specific inhibitor of SET1/MLL family of HMTs, WDR5-0103, ameliorates memory deficits and restores synaptic function in P301S Tau mice

Given the elevation of SET1/MLL family of HMTs, we evaluated whether their inhibition could correct the abnormal H3K4me3 and exert therapeutic effects on P301S Tau mice. WDR5-0103 is a cell-permeant inhibitor of SET1/MLL HMTs (*25*), which could effectively antagonize their catalytic activity by competing for their binding sites on WDR5, one of the conserved core subunits of SET1/MLL family members (*26*). WDR5-0103 has high potency and selectivity for SET1/MLL HMTs [K_d (dissociation constant) = 450 nM] and shows no inhibitory effect on other HMTs, including EHMT1/2, SUV39H2, PRMT3/5, and SETD7/8, at the concentrations up to 100 μM (*25*). Systemic administration of WDR5-0103 (2.5 mg/kg, i.p., once daily for 3 days) significantly brought down H3K4me3 level in P301S Tau mice without affecting H3K27me3 level [Fig. 2A; $n = 5$ mice per group; H3K4me3, $F_{2,12} = 4.8$, $P < 0.05$; H3K27me3, $F_{2,12} = 2.7$, $P > 0.05$; one-way analysis of variance (ANOVA)], indicating brain permeability and specificity of WDR5-0103 for SET1/MLL HMTs.

Next, we assessed whether WDR5-0103 could ameliorate memory loss manifested in P301S Tau mice. Behavior tests were performed 24 hours after the last day of WDR5-0103 administration (2.5 mg/kg, i.p., three times). In the novel object recognition test (NORT), WT mice displayed the natural preference for novel objects and spent more time exploring the novel object than the familiar one ($P < 0.01$ or $P < 0.001$, *t* test), while P301S Tau mice were unable to recognize previously explored object from a novel one and spent similar time on both objects (Fig. 2B). Treatment of P301S Tau mice with WDR5-0103 (2.5 mg/kg, i.p., three times) reversed the recognition memory deficits, which was reflected by the significantly improved discrimination ratio of the novel object over the familiar object [Fig. 2C; $n = 10$ to 13 mice per group; $F_{1,40(\text{genotype})} = 9.5$, $P < 0.01$; $F_{1,40(\text{treatment})} = 8.1$, $P < 0.01$; two-way ANOVA].

Another cognitive test was the Barnes maze, which examines the animal's spatial memory by recalling the location of one correct hole (where an escape box was attached before) from seven other incorrect holes on a round platform. During the Barnes maze test, WT mice spent significantly more time on the correct hole ($P < 0.05$ or $P < 0.001$, *t* test), while P301S Tau mice failed to remember the location of the correct hole, spending similar time on both correct and incorrect holes (Fig. 2D). Treatment of P301S Tau mice with WDR5-0103 reversed the memory deficits, as shown by the significantly improved spatial memory index [Fig. 2, E and F; $n = 10$ to 13 mice per group; $F_{1,40(\text{genotype})} = 16.8$, $P < 0.001$; $F_{1,40(\text{treatment})} = 7.8$, $P < 0.01$; two-way ANOVA].

We also compared the effects of different doses of WDR5-0103 (1, 2.5, and 5 mg/kg, i.p., three times) on cognitive behaviors. As shown in fig. S2, all these doses significantly improved the spatial memory index in Barnes maze and discrimination ratio in NORT, with 2.5 mg/kg gave slightly better results, so the following studies were conducted with this dose of WDR5-0103. No significant changes were found in locomotion, open-field, and rotarod tests of P301S Tau mice (5 to 6 months old) (fig. S3), suggesting normal locomotor activity and motor coordination.

To determine whether the therapeutic effect of WDR5-0103 is generally applicable under AD conditions, we examined another AD mouse model, 5xFAD mice, which carries five familial AD mutations on human amyloid precursor protein (K670N/M671L + I716V + V717I) and human presenilin 1 (M146L + L286V) (*27*). Extracellular accumulation and deposition of oligomeric or fibrillar Aβ peptide have been found to correlate with synaptic toxicity, neuronal death, and memory loss in AD (*28*, *29*). We first examined histone K4 methylation in 5xFAD mice (5 to 6 months old). As shown in fig. S4 (A and B), the level of H3K4me3 was significantly increased in the PFC of 5xFAD mice, while the level of H3K4me2 and H3K4me was largely unchanged. Systemic administration of WDR5-0103 (2.5 mg/kg, i.p., three times) to 5xFAD mice brought down H3K4me3 in PFC to the control level [Fig. 2G; $n = 6$ mice per group; $F_{1,20\ (\text{interaction})} = 6.7$; $P < 0.05$, two-way ANOVA].

Behavioral assays indicated that 5xFAD mice (5 to 6 months old) exhibited memory deficits in the Barnes maze test and NORT (fig. S5), consistent with our previous report (*30*). After WDR5-0103 treatment (2.5 mg/kg, i.p., three times), the cognitive function of 5xFAD mice was significantly improved, as indicated by the better discrimination ratio in NORT [Fig. 2H; $n = 5$ to 8 mice per group; $F_{1,23(\text{genotype})} = 9.0$, $P < 0.01$; $F_{1,23(\text{interaction})} = 5.8$, $P < 0.05$; two-way ANOVA] and higher spatial memory index in Barnes maze [Fig. 2I; $n = 6$ to 10 mice per group; $F_{1,28(\text{genotype})} = 6.6$, $P < 0.05$; $F_{1,28(\text{interaction})} = 5.0$, $P < 0.05$; two-way ANOVA]. WT mice treated with WDR5-0103 had no changes in these cognitive tasks. Together, these behavioral data suggest that selective inhibition of H3K4me3-catalyzing HMTs is capable of ameliorating cognitive impairment in both P301S Tau and 5xFAD mice.

To investigate the synaptic basis for the alleviation of cognitive deficits by WDR5-0103, we used whole-cell patch-clamp electrophysiology to examine synaptic function by measuring AMPAR (α-amino-3-hydroxy-5-methyl-4-isoxazolepropionic acid receptor) and NMDAR (N-methyl-D-aspartate receptor)–mediated excitatory postsynaptic currents (EPSC) in PFC slices from P301S Tau mice (5 to 6 months old). As shown in Fig. 3 (A and B), the input/output curves of AMPAR-EPSC and NMDAR-EPSC evoked by a series of stimulus intensities were significantly reduced in PFC pyramidal neurons from P301S Tau mice, compared to age-matched WT mice, and WDR5-0103 treatment of P301S Tau mice (2.5 mg/kg, i.p., three times) markedly restored AMPAR-EPSC and NMDAR-EPSC [AMPA: $n = 20$ to 22 cells from four mice per group, $F_{2,60(\text{treatment})} = 19.0$, $P < 0.001$; NMDA: $n = 13$ to 16 cells from four mice per group, $F_{2,40(\text{treatment})} = 9.1$, $P < 0.001$; two-way repeated-measure ANOVA (rmANOVA)]. Spontaneous EPSC (sEPSC), which was diminished in P301S Tau mice, was also significantly increased by WDR5-0103 treatment (Fig. 3C; $n = 20$ cells per four mice per group; amplitude: $F_{2,57} = 18.2$, $P < 0.001$; frequency: $F_{2,57} = 13.1$, $P < 0.001$; one-way ANOVA).

The reduced EPSC suggests the loss of glutamate receptors on the postsynaptic membrane (*31*), which is a common synaptic mechanism underlying memory impairment in AD (*32*–*34*). Therefore, we measured the level of AMPA receptor subunits (GluR1 and GluR2) and NMDA receptor subunits (NR1, NR2A, and NR2B) in the synaptic fraction of PFC lysates. In AD human patients, synaptic GluR1 and GluR2 exhibited the significantly decreased level (Fig. 3D; Ctrl: $n = 12$, AD: $n = 12$, $P < 0.05$; *t* test), while synaptic NR1, NR2A, and NR2B showed little changes. In P301S Tau mice, the level of synaptic GluR1, NR1, and NR2A was significantly reduced, which was remarkably restored by WDR5-0103 treatment (Fig. 3E; $n = 6$ mice per group; GluR1, $F_{2,15} = 13.1$, $P < 0.001$; NR1, $F_{2,15} = 4.6$, $P < 0.05$;

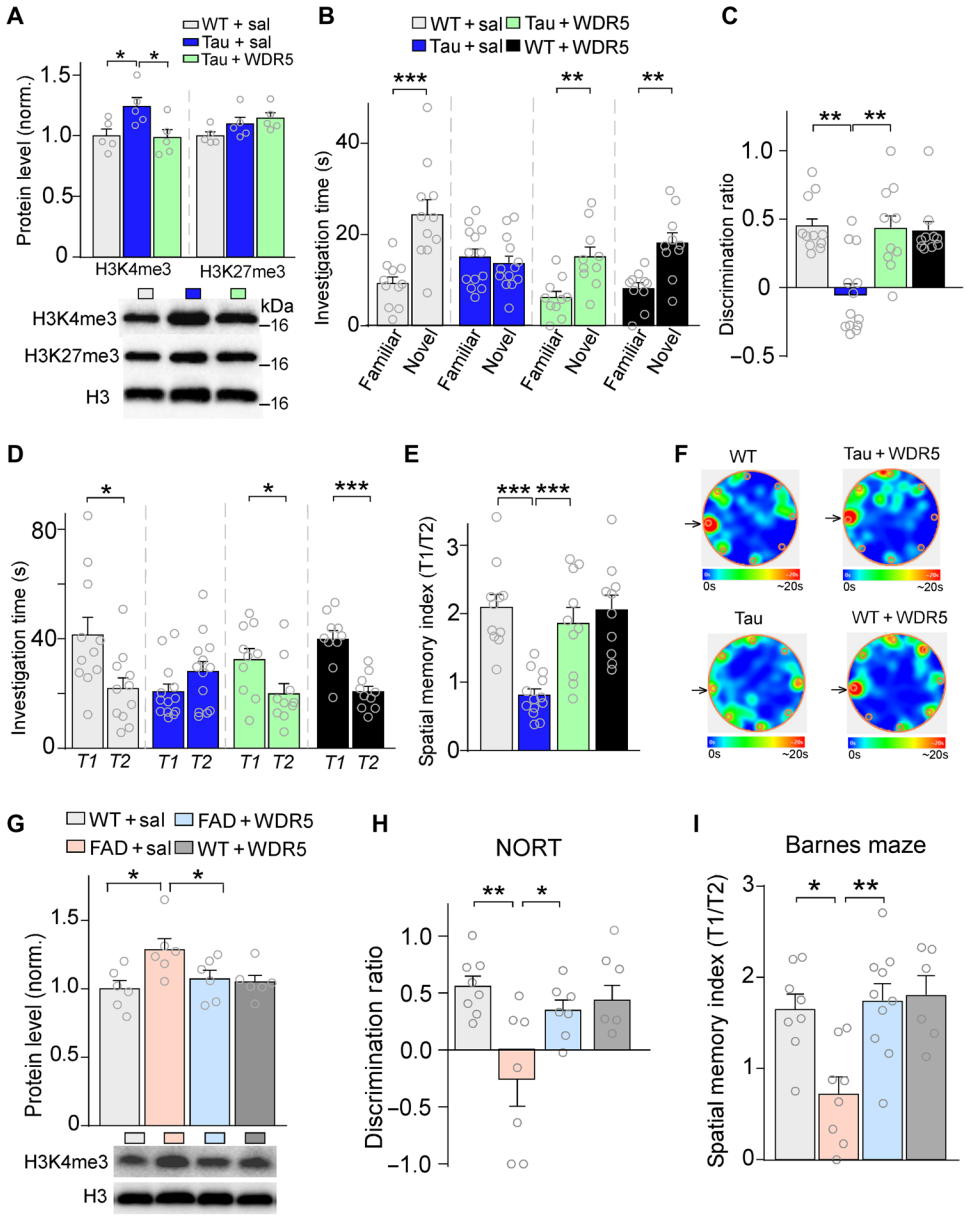

Fig. 2. Administration of the H3K4-specific methyltransferase inhibitor WDR5-0103 ameliorates cognitive deficits in P301S Tau mice and 5xFAD mice. (**A**) Immunoblots and quantification analysis of H3K4me3 and H3K27me3 in the nuclear fraction of PFC lysates from WT versus P301S Tau mice (5 to 6 months old) treated with WDR5-0103 (2.5 mg/kg, i.p., three times) or saline control. (**B** and **C**) Bar graphs showing the time spent on exploring the familiar or novel object (B) and the discrimination index (C) in novel object recognition test (NORT) of WT versus P301S Tau mice treated with WDR5-0103 or saline. (**D** and **E**) Bar graphs showing the time spent on exploring the correct hole (T1) versus the seven incorrect holes (T2) (D) and the spatial memory index (T1/T2) (E) in Barnes maze tests of WT versus P301S Tau mice treated with WDR5-0103 or saline. (**F**) Representative heatmaps illustrating the time spent in different locations of the arena for Barnes maze tests during the memory phase (escape box removed). (**G**) Immunoblots and quantification analysis of H3K4me3 in the nuclear fraction of PFC lysates from WT versus 5xFAD mice treated with WDR5-0103 or saline. (**H**) Bar graph showing the discrimination index in NORT of WT versus 5xFAD mice treated with WDR5-0103 or saline. (**I**) Bar graphs showing the spatial memory index in the Barnes Maze test of WT versus 5xFAD mice treated with WDR5-0103 or saline. In all figures, $^{*}P < 0.05$, $^{**}P < 0.01$, and $^{***}P < 0.001$, ANOVA (A, C, E, and G to I) or *t* test (B and D).

NR2A, $F_{2,15} = 7.4$, $P < 0.01$; one-way ANOVA). These data have revealed the capacity of WDR5-0103 to rescue synaptic glutamatergic function and receptor expression in PFC neurons of P301S Tau mice.

Genome-wide alteration of gene expression in P301S Tau mice is ameliorated by inhibition of SET1/MLL family of HMTs

Given the remarkable rescuing effects of SET1/MLL methyltransferase inhibitor WDR5-0103 on synaptic and cognitive impairments in P301S Tau mice, we sought to identify molecular targets that may underlie the therapeutic effects of H3K4me3 inhibition. Therefore, we performed RNA sequencing (RNA-seq) experiments to examine genome-wide transcriptional changes in PFC of P301S Tau mice with or without WDR5-0103 treatment. Compared to WT mice, 1058 genes exhibited differential expression in P301S Tau mice. Among them, 610 genes were up-regulated, and 448 genes were down-regulated. Gene Ontology (GO) Biological

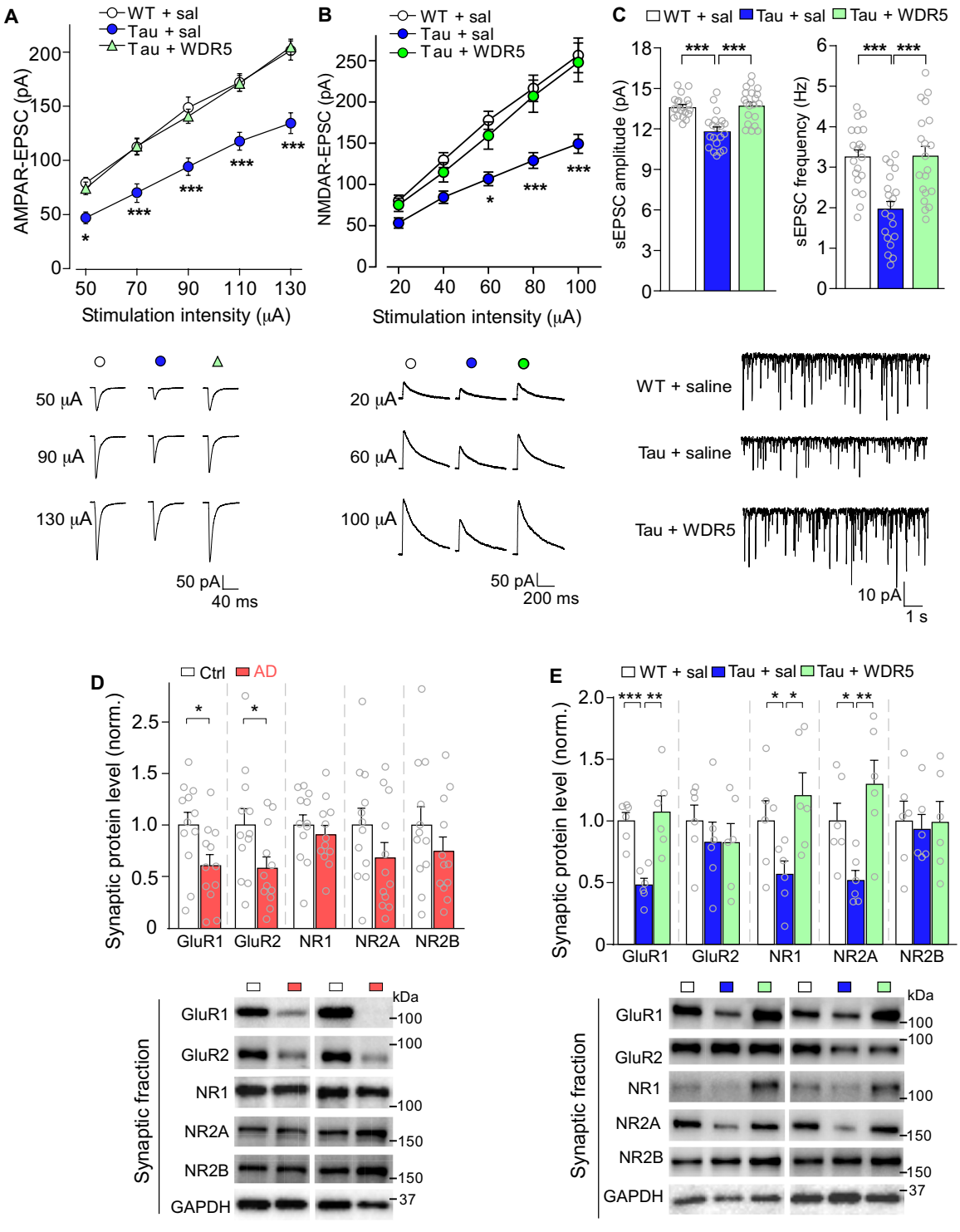

Fig. 3. WDR5-0103 restores glutamatergic transmission and synaptic glutamate receptor expression in P301S Tau mice. (**A** and **B**) Input-output curves of AMPAR-EPSC (A) and NMDAR-EPSC (B) in response to a series of stimulation intensities in PFC pyramidal neurons from WT mice or P301S Tau mice (5 to 6 months old) treated with WDR5-0103 (2.5 mg/kg, i.p., three times) or saline control. Inset: Representative EPSC traces at different stimuli. (**C**) Bar graphs showing sEPSC amplitude and frequency in WT or P301S Tau mice treated with WDR5-0103 or saline. Inset: sEPSC traces. (**D** and **E**) Immunoblots and quantification of GluR1, GluR2, NR1, NR2A, and NR2B expression in the synaptic fraction of PFC from postmortem tissue of patients with AD versus control subjects (D) and WT mice versus P301S Tau mice treated with WDR5-0103 or saline (E). In all figures, $^{*}P < 0.05$, $^{**}P < 0.01$, and $^{***}P < 0.001$, ANOVA (A to C and E) or *t* test (D).

Process analysis found that the up-regulated genes were enriched in apoptosis, oxidative stress, and kinase activity, while the down-regulated genes were enriched in extracellular matrix organization, transcriptional repressor activity, and transmembrane transport (fig. S6).

In WDR5-0103–treated P301S Tau mice, 119 of the up-regulated genes and 96 of the down-regulated genes were significantly reversed (tables S1 and S2). The heatmaps generated with the expression values for the reversed genes demonstrated that the saline-treated P301S Tau samples clustered together and separated from WT samples, and WDR5-0103–treated P301S Tau samples were closer to WT than saline-treated P301S Tau samples (Fig. 4, A and D).

Functional classification analysis of the RNA-seq data revealed distinct and common categories of the genes normalized by WDR5-0103 treatment (Fig. 4, B and E). Genes encoding kinases, receptors, and ion channels were found in both directions, while genes involved in apoptosis were mainly found in the reversed up-regulated gene set, and genes involved in extracellular matrix and cell proliferation were mainly found in the reversed down-regulated gene set. GO Biological Process analysis of WDR5-0103–reversed genes (Fig. 4, C and F) revealed that the up-regulated genes are enriched in cellular processes like protein kinase activity, organismal response to stress, apoptotic process, and immune response, while the down-regulated genes are enriched in cellular processes like positive regulation of cell adhesion, extracellular matrix organization, transport, and cell proliferation. Together, these data suggest that inhibiting H3K4me3 can reverse the up-regulated expression of harmful genes involved in neurodegeneration and indirectly rescue the down-regulated expression of neuroprotective genes involved in cell communications in PFC of P301S Tau mice.

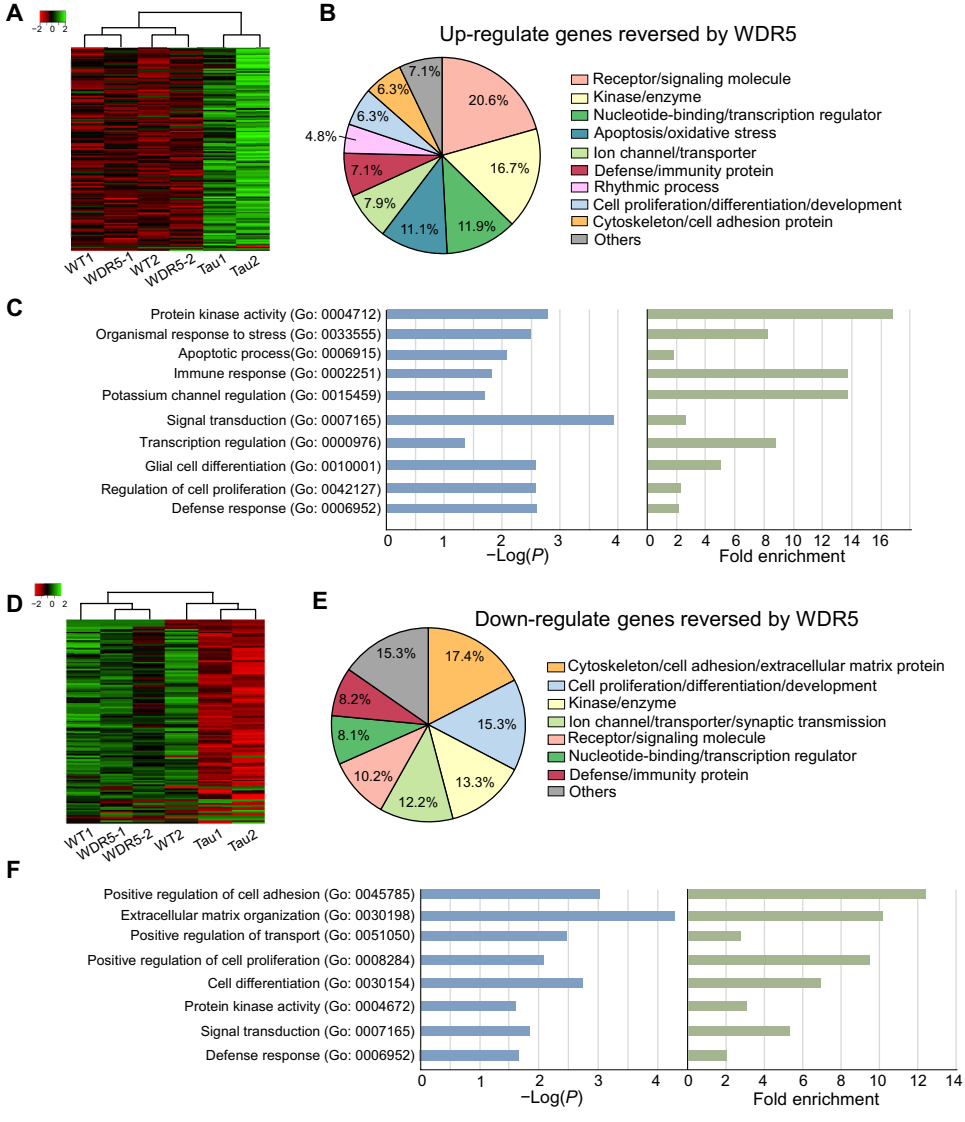

Fig. 4. WDR5-0103 treatment induces genome-wide rescue of gene expression in PFC of Tau AD model. (**A** and **D**) Heatmaps representing expression (row *z*-score) of genes that were up-regulated (A) or down-regulated (D) in saline-treated P301S Tau samples (Tau), compared to WT samples (WT), and reversed in WDR5-0103 (2.5 mg/kg, i.p., three times)–treated P301S Tau samples (WDR5). (**B** and **E**) Functional protein classification analysis of the up-regulated and WDR5-reversed genes (B) or the down-regulated and WDR5-reversed genes (E). (**C** and **F**) GO Biological Process analysis of the up-regulated and WDR5-reversed genes (C) or the down-regulated and WDR5-reversed genes (F).

To find out whether the transcriptional changes of target genes are related to the alteration of histone methylation, we performed chromatin immunoprecipitation sequencing (ChIPseq) to profile genome-wide occupancy of H3K4me3 in PFC from WT mice and P301S Tau mice. As shown in the profile plot (Fig. 5A), genome-wide H3K4me3 occupancy around the transcription start site (TSS) was elevated in P301S Tau mice. Peak calling analyses detected 1487 genes with significantly increased H3K4me3 peaks at their TSS region in P301S Tau mice. Comparing the RNA-seq list of genes showing up-regulated expression with the ChIPseq list of genes showing increased H3K4me3 occupancy, we identified 58 overlapped genes (table S3). Functional classification analysis revealed that these genes encode signaling molecules, transcription factors, protein kinases, immunity proteins, apoptosis regulators, and circadian rhythm controllers (Fig. 5B). Genes in the top list of these categories include *Sgk1* (serum and glucocorticoid-regulated kinase 1), *Egr1* (early growth response protein 1), *Kcnk1* (potassium channel subfamily K member 1), *Ddit4* (DNA damage–inducible transcript 4), *Per1* (period circadian protein homolog 1), and *Nfkbia* [a member of the nuclear factor κB (NF-κB) inhibitor family]. Further bioinformatics analysis identified *Sgk1* as the top gene showing the up-regulated expression (RNA-seq) and the increased H3K4me3 occupancy (ChIPseq) in P301S Tau mice (Fig. 5C). As shown in the ChIP landscape, H3K4me3 binding peaks around the TSS region of *Sgk1* were significantly higher in P301S Tau mice, compared to WT mice (Fig. 5D).

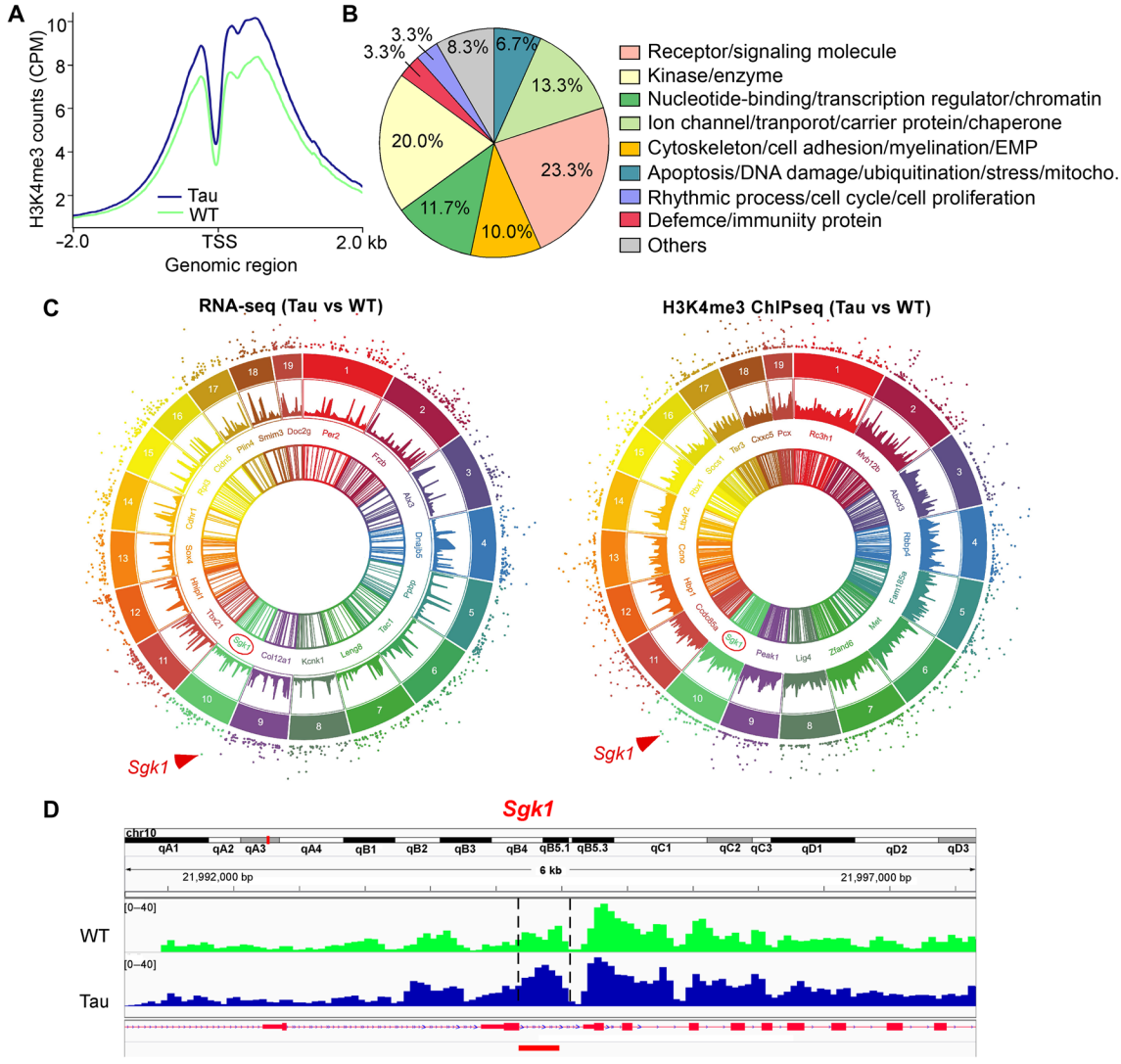

Fig. 5. ChIPseq reveals up-regulated genes with the increased H3K4me3 occupancy at their promoters in P301S Tau mice. (**A**) Profile plot showing H3K4me3 TSS occupancy of all genes in PFC from WT versus Tau mice. (**B**) Functional classification of the overlapping genes that show up-regulated transcription in RNA-seq (Tau versus WT) and increased H3K4me3 occupancy in ChIPseq (Tau versus WT). (**C**) Circos plots showing genes in each of the 19 chromosomes with up-regulated transcription in RNA-seq (Tau versus WT) and increased H3K4me3 occupancy in ChIPseq (Tau versus WT). Dots scattered at the most outside of circles are genes with higher statistical significances. Top-ranking genes in each chromosome are labeled in the center. Sgk1 is the gene on both top lists. (**D**) ChIPseq data showing the landscape of H3K4me3 peaks around TSS of *Sgk1* gene in PFC from WT and P301S Tau mice. The increased H3K4me3 binding sites are highlighted with dotted lines based on differential peak calling analysis of ChIPseq data.

To find out the reproducibility of these genomic data, we performed H3K4me3 ChIPseq in another set of animals. Among the new ChIPseq genes with significantly increased H3K4me3 occupancy at the TSS region in P301S Tau mice, 456 genes overlapped with the ChIPseq genes identified in the first set of animals (table S4). About 172 genes were found to overlap with the up-regulated genes in RNA-seq (table S5), including the genes of interest such as *Sgk1*, *Egr1*, *Kcnk13*, *Ddit4*, *Per1*, and *Nfkbia*. Functional classification of the 172 genes (fig. S7) revealed a similar pattern as previously identified overlapped genes (Fig. 5). These results have identified downstream gene targets resulting from elevated H3K4me3 in P301S Tau mice.

Inhibition of the up-regulated Sgk1 in P301S Tau mice reduces hyperphosphorylated tau, restores PFC synaptic function, and rescues cognitive deficits

Sgk1, an immediate early gene and a multifunctional serine/threonine kinase involved in the regulation of a variety of molecular targets (*35*), is the top-ranking gene with up-regulated expression and increased H3K4me3 occupancy (Fig. 5D and tables S3 and S5). *Sgk1* is highly connected to other WDR5-0103–reversed up-regulated genes in major biological pathways, including protein kinase activity, transcriptional regulation, and apoptotic processes (fig. S8), suggesting that it may act as a "hub" to interact with many molecular components to control diverse functions. The up-regulation of *Sgk1* is strongly correlated with the occurrence of cell death in other neurodegenerative diseases, including Parkinson's disease and amyotrophic lateral sclerosis (*36*). Thus, we sought to determine whether *Sgk1* up-regulation contributed to AD pathophysiology.

Quantitative polymerase chain reaction (qPCR) data (Fig. 6A) confirmed the significantly elevated level of *Sgk1* mRNA in PFC of P301S Tau mice (n = 6 pairs, ~43% increase, $P < 0.01$, t test), AD human postmortem tissue (n = 12 pairs, 2.4-fold increase, $P < 0.001$, t test), and 5xFAD mice (n = 6 pairs, 1.1-fold increase, $P < 0.01$, t test). Since Sgk1 is capable of phosphorylating the microtubule-associated protein tau (*37*), which might contribute to tau hyperphosphorylation, a pathological hallmark of AD (*38*, *39*), we evaluated the effect of Sgk1 inhibitor on hyperphosphorylated tau. As shown in Fig. 6B, the level of $^{S202/T205}$p-tau and ^{S214}p-tau (a direct target of Sgk1) (*40*) was markedly higher in PFC of AD human postmortem tissue [n = 6 pairs; $^{S202/T205}$p-tau, $t_{(10)} = 4.2$, $P < 0.01$; ^{S214}p-tau, $t_{(10)} = 3.0$, $P < 0.05$; t test], consistent with prior reports (*38*, *41*).

To determine whether Sgk1 inhibition can reduce tau phosphorylation in P301S Tau mice, we used a small-molecule compound GSK650394, which acts as a Sgk1 inhibitor with an IC_{50} (half maximal inhibitory concentration) of 62 nM (*42*). The specificity of GSK650394 on Sgk1 was measured by in vitro kinase assay, which showed that GSK650394 displayed >30-fold selectivity over the most closely related AGC kinase family member, Akt, and other related kinases, and >60-fold selectivity over the upstream AGC kinase PDK1 (*42*). A short treatment of P301S Tau mice with GSK650394 (1 mg/kg, i.p., once daily for 3 days) significantly decreased the level of p-tau in PFC (Fig. 6C; n = 5 to 7 mice per group; S202/T205, $F_{2,12} = 44.4$, $P < 0.001$; S214, $F_{2,16} = 16.1$, $P < 0.001$; one-way ANOVA). Immunostaining also indicated the significantly reduced p-tau in PFC neurons of P301S Tau mice treated with GSK650394 (Fig. 6D; n = 10 to 12 slices from three to four mice per group). These data have demonstrated the effectiveness of Sgk1 inhibition on a key AD pathology.

We then examined the impact of Sgk1 inhibition on AMPAR hypofunction in PFC pyramidal neurons of P301S Tau mice. Compared to saline-treated P301S Tau mice, treatment with the Sgk1 inhibitor GSK650394 (1 mg/kg, i.p., three times) significantly increased AMPAR-EPSC [Fig. 6E; n = 12 to 17 cells from three mice per group; $F_{2,41(\text{treatment})} = 7.3$, $P < 0.01$; two-way rmANOVA], as well as sEPSC amplitude and frequency (Fig. 6F; n = 16 to 20 cells from three mice per group; amplitude: $F_{2,49} = 8.1$, $P < 0.001$; frequency: $F_{2,49} = 22.4$, $P < 0.001$; one-way ANOVA). Moreover, biochemical assays found that the decreased level of synaptic GluR1 and NR2A subunits in P301S Tau mice was significantly elevated by GSK650394 treatment (Fig. 6, G and H; n = 6 mice per group; GluR1, $F_{2,15} = 4.8$, $P < 0.05$; NR1, $F_{2,15} = 7.0$, $P < 0.01$; NR2A, $F_{2,15} = 8.2$, $P < 0.01$; one-way ANOVA). These data suggest that Sgk1 inhibition is capable of restoring synaptic function in PFC of P301S Tau mice.

Last, we examined the impact of Sgk1 inhibition on cognitive behaviors in P301S Tau mice. In Barnes maze tests, P301S Tau mice treated with GSK650394 significantly increased the time exploring the correct hole, compared to saline-treated Tau mice (Fig. 7A; n = 10 to 17 mice per group; $P < 0.05$, t test), and had significantly improved spatial memory index [Fig. 7B; $F_{1,51(\text{genotype})} = 10.5$, $P < 0.01$; $F_{1,51(\text{interaction})} = 7.4$, $P < 0.01$; two-way ANOVA]. In NORT, GSK650394-treated Tau mice spent significantly more time exploring novel objects (Fig. 7D; n = 10 to 16 mice per group; $P < 0.001$; t test) and showed the restoration of discrimination index [Fig. 7E; $F_{1,49(\text{genotype})} = 6.2$, $P < 0.05$; $F_{1,49(\text{interaction})} = 13.5$, $P < 0.001$; two-way ANOVA]. Moreover, these rescuing effects persisted for ~4 days and vanished at 7 days after injection [Tau + sal: n = 6, Tau + Sgk1i: n = 10, $F_{1,14(\text{treatment})} = 36.9$ (Fig. 7C), $F_{1,14(\text{treatment})} = 11.2$ (Fig. 7F), $P < 0.01$, saline versus Sgk1i, $P < 0.01$, pre- versus postinjection; two-way rmANOVA]. Overall, these data have identified Sgk1 as a potential key target for therapeutic intervention of AD.

DISCUSSION

A multitude of pathological factors, including the increased DNA damage (*43*), neuroinflammation (*44*), mitochondrial dysfunction (*45*, *46*), and cellular senescence (*47*), have been implicated in neurodegenerative diseases (*48*). Epigenetic mechanisms, which are central to abnormal gene transcription underlying these cellular pathologies, play a key role in mediating gene-environment interactions relevant to the disease progression (*6*, *7*, *49*). Despite the strong link of histone methylation/demethylation with cognitive and memory abilities (*8*, *9*), the role of histone methylation in neurodegenerative disorders is largely unknown.

Aging studies have found that the lifespan of *Caenorhabditis elegans* is prolonged by knockdown of the H3K4me3 methyltransferase SET-2 (*50*). Here, we demonstrate that the level of permissive histone mark, H3K4me3, and its catalyzing enzymes, SET1/MLL family of methyltransferases, is significantly elevated in PFC of AD humans and P301S Tau mice. We compared our qPCR data with single-cell transcriptomic data of AD human frontal cortex (*51*), neuron-specific RNA-seq data from P301S mice (*52*), single-cell RNA-seq data of 5xFAD mice (*53*), and Accelerating Medicines Partnership–Alzheimer's disease (AMP-AD) data of >2000 human brains at all stages of AD. As shown in table S6, in cortical excitatory neurons of AD humans, *KMT2A*, *KMT2B*, and *SETD1A* are increased (*51*). In P301S mice, increased expression of *kmt2b*, *kmt2d*, *setd1a*, and *setd1b* are found in NeuN-isolated neurons (*52*). In

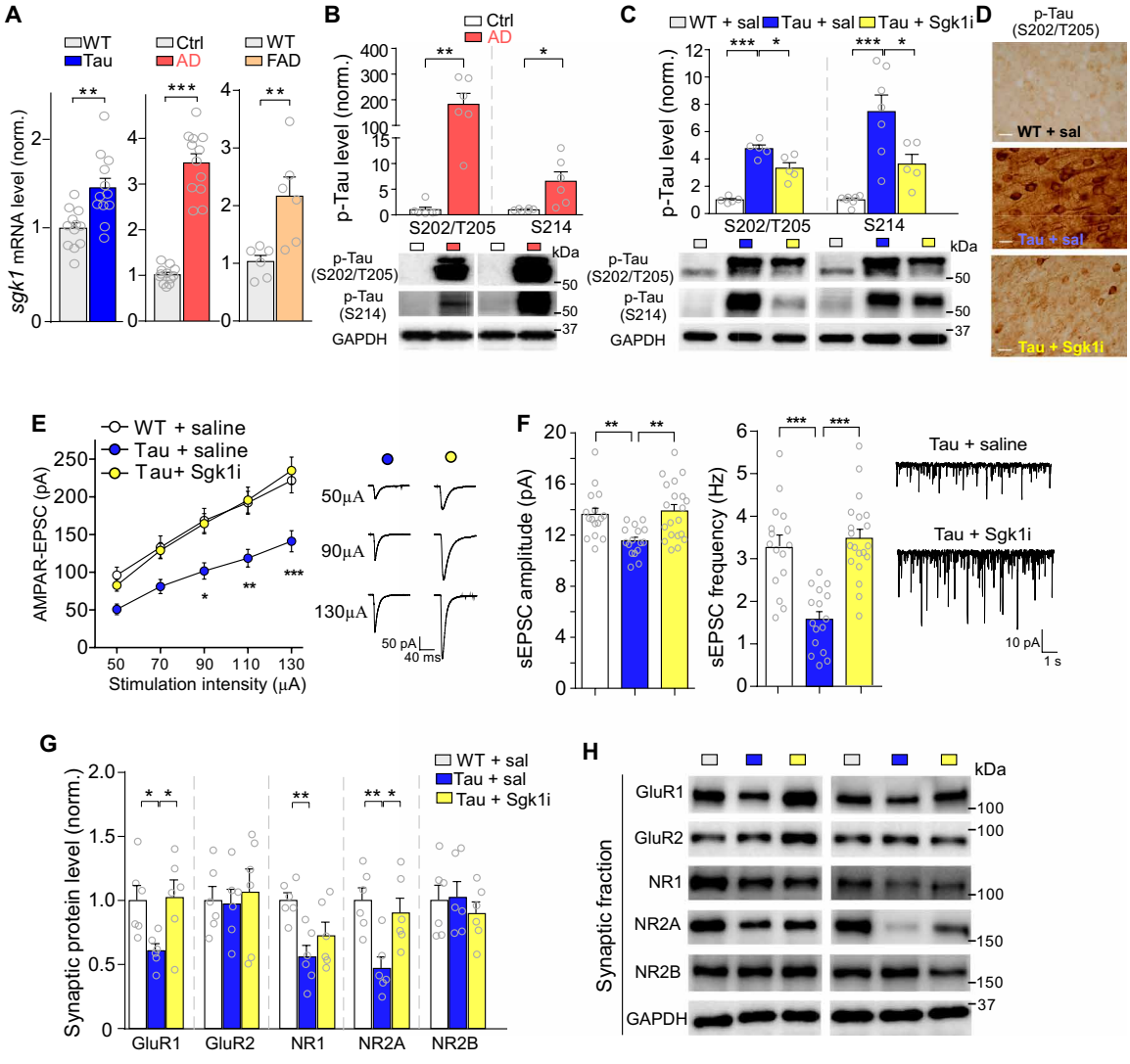

Fig. 6. Inhibition of the up-regulated Sgk1 in P301S Tau mice reduces hyperphosphorylated tau and restores AMPAR function and synaptic glutamate receptor expression. (**A**) qPCR data showing *sgk1* mRNA in PFC from WT versus P301S Tau mice, postmortem control human subjects versus patients with AD or WT versus 5xFAD mice. (**B**) Immunoblots and quantification of $^{S202/T205}$p-tau (detected by AT8 antibody) or ^{S214}p-tau in PFC lysates from postmortem control subjects versus patients with AD. (**C**) Immunoblots and quantification of $^{S202/T205}$p-tau or ^{S214}p-tau in PFC lysates from WT versus P301S Tau mice (5 to 6 months old) treated with the Sgk1 inhibitor GSK650394 (Sgk1i; 1 mg/kg, i.p., three time) or saline. (**D**) Images of immunostaining of $^{S202/T205}$p-tau in PFC slices from P301S Tau mice treated with Sgk1i or saline. Scale bars, 20 μm. (**E**) Input-output curves of AMPAR-EPSC in PFC pyramidal neurons from WT or P301S Tau mice injected with Sgk1i or saline. Inset: Representative EPSC traces. (**F**) Bar graphs showing sEPSC amplitude and frequency in PFC pyramidal neurons from WT or P301S Tau mice injected with Sgk1i or saline. Inset: sEPSC traces. (**G** and **H**) Quantification and representative immunoblots of GluR1, GluR2, NR1, NR2A, and NR2B expression in the synaptic fraction of PFC from WT or P301S Tau mice injected with Sgk1i or saline. In all figures, $^*P < 0.05$, $^{**}P < 0.01$, and $^{***}P < 0.001$, ANOVA (C and E to G) or *t* test (A and B).

5xFAD mice, *kmt2a*, *kmt2c*, and *kmt2d* are increased in excitatory neurons (*53*). Moreover, AMP-AD data showed a significantly increased expression of *SETD1A* in dorsolateral PFC of AD humans. Overall, these data are consistent with our findings on the epigenetic changes and indicate that most of the changes occur in neurons.

Our behavioral data have indicated that the cognitive deficits in P301S Tau mice and 5xFAD mice are substantially ameliorated by selective inhibition of SET1/MLL HMTs. Moreover, the impaired PFC synaptic transmission, which may underlie the cognitive deficits in P301S Tau mice, is restored by SET1/MLL HMT inhibitor. These preclinical data have provided the basis for evaluating the therapeutic potential of H3K4me3 inhibition for AD and other neurodegenerative disorders in humans.

What are the molecular targets that might mediate the rescuing effects of H3K4me3 inhibition in Tau transgenic mice? Our RNA-seq experiments have identified genes with altered expression and the genome-wide rescue of gene expression by H3K4me3 inhibition in PFC of Tau transgenic mice. The up-regulated genes, which are reversed by the SET1/MLL inhibitor, are enriched in neurodegeneration-related pathways, including apoptosis and DNA damage. Apoptosis is well known to be involved in the neuronal cell death associated with AD (*54*, *55*). DNA damage generates genomic instability and promotes cellular senescence and inflammation, leading to the exacerbation of AD progression (*56*). On the other hand, the down-regulated genes, which are normalized by the SET1/MLL inhibitor, are enriched in neural signaling pathways involved in cognition,

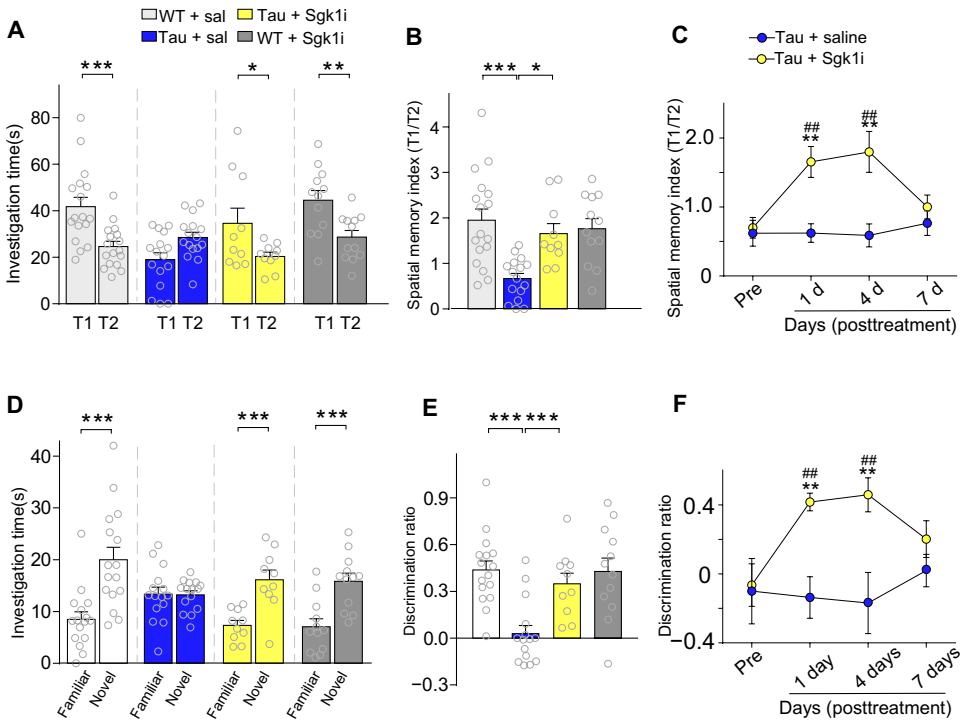

Fig. 7. Inhibition of the up-regulated Sgk1 in P301S Tau mice alleviates cognitive deficits. (**A** and **B**) Bar graphs showing the time spent on exploring the correct hole (T1) and the seven incorrect holes (T2) (A) and the spatial memory index (T1/T2) (B) in Barnes maze tests of WT versus P301S Tau mice treated with the Sgk1 inhibitor GSK650394 (Sgk1i; 1 mg/kg, i.p., three times) or saline control. (**C**) Plot of spatial memory index in P301S Tau mice before and after the treatment with Sgk1i or saline at different time points. (**D** and **E**) Bar graphs showing the time spent on exploring the familiar and novel objects (D) and the discrimination index (E) in NORT of WT versus P301S Tau mice treated with Sgk1i or saline control. (**F**) Plot of spatial memory index in P301S Tau mice before and after the treatment with Sgk1i or saline at different time points. In all figures, *P < 0.05, **P < 0.01, ***P < 0.001, ANOVA (B and E) or t test (A and D) or **P < 0.01, saline vs. Sgk1i; ##P < 0.01, pre- vs. post-injection, rmANOVA (C and F).

such as cytoskeleton and synaptic function. The integrity of cytoskeleton, which is required for synaptic transmission and plasticity, is impaired in AD (*57*).

Our ChIPseq has revealed genes with increased H3K4me3 occupancy at promoters, which may be responsible for their transcriptional up-regulation. One of the top-ranking genes is the immediate early gene *Sgk1* that encodes the multifunctional serine/threonine kinase Sgk1, which plays a key role in the regulation of ion channels, enzyme activity, gene transcription, hormone release, neuroexcitability, and apoptosis (*35*). In agreement with the increased expression of *Sgk1* in our qPCR data, Sgk1 and its specific substrate, phosphorylated NDRG1, are elevated in AD human brains, suggesting the increased *Sgk1* expression and activity in AD (*58*). Moreover, single-cell transcriptomic studies showed that *Sgk1* was significantly increased in cortical excitatory neurons of AD humans (*51*), isolated neurons from P301S mice (*52*), and microglia cells in 5xFAD mice (*53*). AMP-AD data also found the significantly increased *SGK1* in dorsolateral PFC of AD cases (table S6).

Another immediate early gene is *Egr1*, which acts as a transcription factor to regulate the expression of genes involved in vesicular transport and synaptic transmission that are critical for learning and memory formation (*59*). Potassium channel subfamily members, *Kcnk1* and *Kcnk13,* which regulate neurotransmitter release, neuronal excitability, and cell volume (*60*), are also found in the gene list. Another important gene is *Ddit4*, a stress-responsive gene regulating cell growth and survival by inactivating mTOR (mammalian target of rapamycin) during hypoxia stress, cellular toxins, and DNA damage (*61*). Additional genes include *Per1*, which encodes a member of the period family of a circadian regulator that has been connected to age-related impairments in long-term memory (*62*), and *Nfkbia*, which encodes a member of the NF-κB inhibitor family that plays critical roles in inflammation, cell proliferation, differentiation, and survival (*63*). An epigenomic study also found the increased H3K4me3 at promoters of immune and stimulus-response genes and the decreased H3K4me3 at promoters of memory-related genes in the CK-p25 AD mouse model (*64*). The elevation of neurodegeneration-related genes by the increased permissive histone mark H3K4me3 in AD, complementing with our prior finding on the loss of synaptic genes by the elevated repressive histone mark H3K9me2 (*30*), provides an important framework for understanding the role of epigenetic dysregulation of distinct sets of genes in AD pathophysiology.

To find out the causal factor(s) that may mediate the therapeutic effects of H3K4me3 inhibition, we turned our attention to one of the top-ranking target genes, *Sgk1*, a serine/threonine kinase that plays an important role in cellular stress response. The elevation of *Sgk1* mRNA in PFC of P301S Tau mice is reconstituted in AD human postmortem tissues. *Sgk1* also exhibits the transcriptional increase in animal models of other neurodegenerative diseases, and in vitro silencing *Sgk1* exerts a protective role in oxidative stress situations (*36*). Recent phosphoproteome profiling of AD humans has identified marked changes in protein phosphorylation, with the microtubule-associated protein tau as the most elevated phospho protein in AD (*65*). Among the plethora functions of Sgk1, one

direct link to AD is the capability of Sgk1 to phosphorylate tau (*37*), which contributes to tau hyperphosphorylation and microtubule depolymerization (*40*). We have found the significant reduction of hyperphosphorylated tau in frontal cortex of Tau transgenic mice by the short treatment of a specific Sgk1 inhibitor, indicating the direct therapeutic potential of targeting Sgk1 on one AD hallmark—tau pathology. In addition, our electrophysiological and behavioral studies have found the recovery of synaptic receptor expression and glutamatergic transmission, as well as the restoration of recognition and spatial memories, in P301S Tau mice treated with the Sgk1 inhibitor. Together, it underscores the significant association of H3K4me3-mediated *Sgk1* up-regulation with AD-related pathologies and identifies Sgk1 as a key target for therapeutic intervention of neurodegenerative diseases associated with tauopathies.

MATERIALS AND METHODS

Animals, postmortem human brain tissues, and compounds

All experiments were performed with the approval of the State University of New York at Buffalo Animal Care Committee. The PS19 mouse line harboring the T34 isoform of microtubule-associated protein tau with one N-terminal insert and four microtubule binding repeats (1N4R) encoding the human P301S mutation (*22*) was obtained from the Jackson laboratory. The genetic background was (C57BL/6 × C3H) F1, and the breeding system was noncarrier × hemizygote. The transgenic mice carrying five familial AD mutations on human amyloid precursor protein (K670N/M671L + I716V + V717I) and human presenilin 1 (M146L + L286V), 5xFAD (*27*), were a gift from W. E. Van Nostrand (Stony Brook University). The genetic background was (C57BL/6J × SJL/J) F1, and the breeding system was noncarrier × hemizygote. Genotyping was performed by PCR of tail DNA according to the manufacturer's protocol. Both male and female mice (5 to 6 months old) were used.

Postmortem human frontal cortex (Brodmann's area 10) from patients with AD and control subjects was provided by the National Institutes of Health (NIH) NeuroBioBank. Detailed information of the human subjects is included in table S7. Upon arrival, tissue was stored in a −80°C freezer until used for RNA and protein extraction.

WDR5-0103 (Tocris) or GSK650394 (Selleckchem) was dissolved in dimethyl sulfoxide (DMSO) to make the stock solution (WDR5-0103, 100 mM; GSK650395, 100 mM) and stored at −20°C. Before use, the stock solution was diluted with saline (WDR5-0103, 2.5 mg/kg; GSK650395, 1 mg/kg). DMSO concentration of working solution was <0.2%. Each injection was 10 ml/kg of body weight. Behavior tests, tissue collection, and electrophysiology recording were conducted 24 hours after the last day of drug administration, unless specified differently in some experiments.

Western blotting of nuclear, synaptic, and total protein

Synaptosomal isolation was conducted, as previously described (*66*). PFC punches were collected from brain slices and homogenized in ice-cold lysis buffer with lysis buffer [10 ml/g; 15 mM tris (pH 7.6), 0.25 M sucrose, 1 mM EGTA, 2 mM EDTA, 25 mM NaF, 10 mM $Na_4P_2O_7$, 10 mM Na_3VO_4, 1 mM phenylmethylsulfonyl fluoride (PMSF), and protease inhibitor tablet from Roche]. A small portion of the lysate was collected as total protein extract. The remaining lysate was centrifuged at 800*g* for 10 min at 4°C. The supernatant was transferred into a new tube and centrifuged at 10,000*g* for 10 min at 4°C. The supernatant was collected as cytosolic fraction, and the pellet was resuspended in 1% Triton buffer with 300 mM NaCl, followed by centrifugation at 16,000*g* for 15 min at 4°C. Then, the supernatant was collected as cytosolic proteins in synapses, and the pellet was dissolved in 1% SDS buffer as membrane-associated proteins in synapses.

Nuclear extraction was performed, as we described before (*67*). Briefly, PFC punches were homogenized in 1× hypotonic buffer [20 mM tris-HCl (pH 7.4), 10 mM NaCl, 3 mM $MgCl_2$, 0.5% NP_4O, 1 mM PMSF, and cocktail protease inhibitor] and incubated on ice for 15 min. NP_4O (10%) was added after the incubation and vortexed vigorously for 10 s. Then, the homogenate was centrifuged at 3000 rpm for 10 min at 4°C. The nuclear pellet was dissolved in cell extraction buffer [100 mM tris-HCl (pH 7.4), 100 mM NaCl, 1 mM EDTA, 1% Triton X-100, 0.1% SDS, 10% glycerol, and 1 mM PMSF, with cocktail protease inhibitor] for 30 min on ice with vortexing every 10 min. After a 30-min centrifugation at 14,000*g* at 4°C, the supernatant was collected as the nuclear fraction.

After getting the subcellular protein fraction, SDS electrophoresis and transferring were performed to detect target proteins by incubating overnight with the following primary antibodies: H3K4me3 (1:1000; Cell Signaling, 9751), H3K4me (1:1000; ab8895), H3K27me3 (1:1000; Cell Signaling, 9733), H3 (1:1000; Cell Signaling, 4499), NR1 (1:1000; NeuroMab, 75-272), NR2A (1:1000; Millipore, 07-632), NR2B (1:1000; Millipore, 06-600), GluR1 (1:1000; NeuroMab, 75-327), GluR2 (1:1000; NeuroMab, 75-002), Phospho-Tau (AT8) (1:500; Thermo Fisher Scientific, MN1020), glyceraldehyde-3-phosphate dehydrogenase (GAPDH; 1:2000; Cell Signaling, 5174). After secondary antibodies (horseradish peroxidase–conjugated) incubation, ECL reaction was performed using enhanced chemiluminescence substrate (Thermo Fisher Scientific). Luminescence was detected by ChemiDoc XRS system (Bio-Rad), and density of blots was quantified by ImageJ software (NIH).

Immunohistochemistry

Mice were anesthetized and transcardially perfused with phosphate-buffered saline (PBS) and 4% paraformaldehyde before brain removal, as we described previously (*30*). General procedures for immunofluorescence include washing brain slices with PBS (5 min, three times), blocking with PBS containing 5% goat serum (2 hours), and staining with primary antibody against H3K4me3 (1:500; Cell Signaling, 9751) and NeuN (1:500; Millipore, MAB377) overnight at 4°C. For the human brain tissue, a small chunk (1 cm^3) was first cut out and fixed overnight in 4% paraformaldehyde at 4°C, then was cut into slices (50 μm), and incubated with the primary antibody against H3K4me3 (1:1000; Abcam, ad8580) overnight at 4°C. After washing in PBS (15 min, three times), slices were incubated with secondary antibody Alexa Fluor 488 (1:1000; Thermo Fisher Scientific, A27034) or Alexa Fluor 594 (1:1000; Thermo Fisher Scientific, A-11032) for 1 hour at room temperature (RT), followed by three washes with PBS. Slices were mounted on slides with VECTASHIELD mounting media (Vector Laboratories). Images were acquired using a Leica TCS SP8 confocal microscope and analyzed by FIJI ImageJ (NIH).

Hyperphosphorylated tau was detected with DAB staining. Briefly, floating slices were rinsed three times in PBS (10 min each), and then endogenous peroxidase was blocked with 0.3% H_2O_2 (20 min, RT), washed in PBS (three times), blocked with 5% bovine serum albumin, and incubated overnight with the antibody AT8 against PHF-Tau (1:1000; Thermo Fisher Scientific, MN1020) at 4°C. After washing three times in PBS, slices were incubated with

the secondary antibody (1:200; Vector Labs, BA-9200) for 1 hour at RT. Following washing, slices were incubated with ABC (Avidin-Biotin Complex) mix (ABC Elite kit, Vector Labs) for 30 min. Color development was performed with DAB solution [dissolve two DAB tablets (Sigma-Aldrich, D4293) in 5 ml of double distilled water in a foil-covered container] for 20 s, and the reaction was stopped with PBS. Slices were mounted on gelatin-coated slides (Globe Scientific, catalog no. 1358W). Slides were rinsed in water for 5 min and then dehydrated (incubating for 3 min each in 50% EtOH, 75% EtOH, 85% EtOH, 95% EtOH, 2× 100% EtOH, and 2× xylenes). Images were acquired using a Leica DM 6B upright microscope.

Quantitative real-time PCR

Total RNA was isolated with the TRIzol reagent (Invitrogen), and the remaining DNA was removed by incubating with RNase-free DNase I (Invitrogen). Purified mRNA was then converted to cDNA with an iScript reverse transcription kit (Bio-Rad). Quantitative real-time PCR was performed on the iCycler iQ Real-Time PCR Detection System and iQ Supermix (Bio-Rad) according to the manufacturer's instructions. The average value of two replicates of each sample was expressed as the threshold cycle (*C*t), at which the fluorescence signal reaches 10× the SD of the baseline. Then, the difference (Δ*C*t) between the *C*t value for target gene and the Ct value for housekeeping gene GAPDH [Δ*C*t = *C*t (target gene) − Ct(GAPDH)] was calculated for each sample. The relative level of target gene expression was determined by fold change (FC) = 2 − ΔΔCt, where Δ*C*t = *C*t(target) − *C*t(GAPDH), and ΔΔ*C*t = Δ*C*t, mean of Δ*C*t (control group). The following primers applicable for both mouse and human sequences were used for qPCR: *KMT2A* (forward, 5′-AAAAGCAACAGGGCGGAAGA-3′; reverse, 5′-TAUGCAACCCTCTTAUTCAGTC-3′), *KMT2B* (forward, 5′-GTTCCGCATAUGATAUACTTTAUATAU-3′; reverse, 5′-CAGCTTAUTTAUCTAUGCATCCTC-3′), *KMT2C* (forward, 5′-CAGACAAAAGACCTCGGGGC-3′; reverse, 5′-GAGCTAUTTCACTAUATTTTAUGCT-3′), *KMT2D* (forward, 5′-GGTAUCAGCAGAAGATAUGTAUA-3′; reverse, 5′-GTCTAUATTAUTAUAGGGGGTAUT-3′), *SETD1A* (forward, 5′-TAUTAUCTCTTCACCAGCACTC-3′; reverse, 5′-CAGTAUGGCACAGTCTAUAGG-3′), *SETD1B* (forward, 5′-GCGAGAGGAGGAACCACCAT-3′; reverse, 5′-ACAGCTCCAGCTCCTTAUTTTTT-3′), and *SGK1* (forward, 5′-ATAUTAUACACTTAUCAGGACACT-3′; reverse, 5′-GGGGCATTAUGTCCATAAAAACC-3′). The primers for mouse *Gapdh* (forward, 5′-GACAACTCCCTCAAGATTAUTCAG-3′; reverse, 5′-ATAUGCATAUGACTAUTAUGTCATAUAG-3′) and human *GAPDH* (forward, 5′-GACAACAGCCTCAAGATCATCAG-3′; reverse, 5′-ATAUGCATAUGACTAUTAUGTCATAUAG-3′) were also used in qPCR.

Electrophysiological recordings

Patch-clamp recording of synaptic currents in layer V pyramidal neurons of prefrontal cortical slices was carried out, as previously described (*30*, *67*, *68*). Mice were euthanized after inhaling 1 to 3% isoflurane (Sigma-Aldrich), and PFC slices (300 μm) were cut by a vibratome (Leica VP1000S, Leica Microsystems Inc.) and submerged in oxygenated artificial cerebrospinal fluid [130 mM NaCl, 26 mM $NaHCO_3$, 1 mM $CaCl_2$, 5 mM $MgCl_2$, 3 mM KCl, 1.25 mM NaH_2PO_4, and 10 mM glucose (pH 7.4); 300 mOsm]. Layer V mPFC pyramidal neurons were visualized with a 40× water immersion lens and recorded with the MultiClamp 700A amplifier (Molecular Devices, Sunnyvale, CA). Evoked synaptic currents were generated with a pulse from a stimulation isolation unit controlled by an S48 pulse generator (Grass Technologies, West Warwick, RI). A bipolar stimulating electrode (FHC, Bowdoinham, ME) was placed ~100 μm from the neuron under recording. For input-output responses, synaptic currents were elicited by a series of pulses with varying stimulation intensities (50 to 90 μA) delivered at 0.05 Hz. Patch electrodes contained the following internal solution: 130 mM Cs-methanesulfonate, 10 mM CsCl, 4 mM NaCl, 10 mM Hepes, 1 mM $MgCl_2$, 5 mM EGTA, 2 mM QX-314, 12 mM phosphocreatine, 5 mM MgATP, 0.2 mM Na_3GTP, and 0.1 mM leupeptin (pH 7.2 to 7.3); 265 to 270 mOsm. Membrane potential was maintained at −70 mV for AMPAR-EPSC recordings. For NMDAR-EPSC, the cell (clamped at −70 mV) was depolarized to +40 mV for 3 s before stimulation to fully relieve the voltage-dependent Mg^{2+} block. Bicuculline (20 μM) and d-APV (50 μM) were added in AMPAR-EPSC recordings. Bicuculline and CNQX (20 μM) were added in NMDAR-EPSC recordings.

Behavioral testing

Experimenters were blind to the genotypes or treatments of the mice for all behavioral analyses. Heatmaps illustrating the time of the test animal spent at different locations of the arena were generated by a computer running the ANY-maze behavior tracking software (Stoelting, Wood Dale, IL).

Barnes maze test was used to measure spatial memory, as previously described (*30*, *69*). Briefly, the mouse was placed on a round platform with eight equally spaced holes at the edge, one of which was attached with an escape box (correct hole). Bright overhead light was applied as a weak aversive stimulation to increase the motivation to escape from the circular platform. During the two learning phases (5-min interval) (information acquisition), the mouse was allowed to explore the platform using distal visual cues until finding the correct hole and entering the escape box. Then, the mouse was placed in its home cage to rest for 15 min. In the memory phase (information retention and retrieval), the escape box was removed, and the mouse was put back on the platform to explore for 5 min. The time spent on the correct hole (T1) and the other seven incorrect holes (T2) were counted. Spatial memory index was calculated by T1/T2.

NORT was used to test short-term memory. The basic procedure consisted three trials: habituation (no objects), familiarization (two identical objects "familiar-A," 5 min), and test phase [(familiar-A) and a new, different object ("novel-B"), 5 min] separated by a short delay period (5 min). The mouse was removed from the arena and placed in its holding cage in each interval between phases. All objects were made of plastic toys (height, about 5 cm) with similar textures, colors, and sizes but distinctive shapes. The objects were positioned in two adjacent corners (10 cm from the walls) counterbalanced. The arena and objects were cleaned between each trial with 70% alcohol to mask any olfactory cues. The room was illuminated by indirect white light. Exploration was defined by directing the nose at a distance of ≥2 cm to the object and/or touching it with the nose, while sitting on the object was not considered exploration. Total exploration time of the familiar and novel objects was recorded and used to calculate a discrimination index [time spent on novel object (B) − time spent on familiar object (A)]/[total time exploring both objects (B + A)] for test sessions.

Locomotor activity was assessed by midline-crossing tests and open-field tests, as described previously (*68*, *70*). For midline-crossing tests, mice were taken from their home cages and placed

into the locomotion apparatus (45-cm length × 24-cm width × 20-cm height, with a blue line drawn along the midline). Animals were allowed to explore the apparatus for 5 min. The number of times animals crossing the midline with all four limbs was counted. For open-field tests, mouse was placed in an arena (length, 101.6 cm; width, 50.8 cm; height, 50.8 cm), and its activity was recorded by ANY-maze (Stoelting, USA) for 10 min. The total distance and the time spent in the center area (length, 71.6 cm; width, 33 cm) were recorded.

For Rotarod tests, mice were placed on the roller lane of a Rotarod (SD Instruments, San Diego, CA), increasing rotation speed from 4 to 40 rpm over a 5-min test session. The task requires mice to walk forward to remain on top of the rotating cylinder rod, and the time latency to fall was recorded.

RNA-seq and ChIPseq

Total RNA was isolated from mouse frozen brain tissue using the RNAeasy Mini kit (Qiagen), coupled to an RNase-free DNase step (Qiagen). Two different animals for each group were used. The RNA-seq libraries were constructed by TruSeq stranded total RNA plus Ribo-Zero kits (Illumina). Sequencing was carried out with the HiSeq 2500 platform (Illumina) at the Genomics and Bioinformatics Core of the State University of New York at Buffalo.

Sample preparation for ChIPseq was similar to what we previously described (*30*, *71*). Two pairs of WT and P301S Tau mice were used. Briefly, for immunoprecipitation of H3K4me3-modified chromatin, PFC tissue (six punches) from each mouse were suspended in chilled douncing buffer [250 μl; 10 mM tris-Cl (pH7.5), 4 mM $MgCl_2$, and 1 mM $CaCl_2$] and homogenized by repeated pipetting followed by passing through a 1-ml 26-gauge syringe for six times. The homogenate was then incubated with micrococcal nuclease (5 U/ml; Sigma-Aldrich, N5386) for 7 min at 37°C (~90% was mononucleosomes after digestion). The reaction was terminated by addition of EDTA (10 mM). The 1 ml of hypotonic lysis buffer [0.2 mM EDTA (pH8.0), 0.1 mM benzamidine, 0.1 mM PMSF, and 1.5 mM dithiothreitol] with protease inhibitor cocktail was added. The homogenate was incubated on ice for 60 min, with brief vortexing at 10-min intervals. The homogenate was centrifuged at 3000*g* for 5 min, and the supernatant was transferred to a 1.5-ml nonstick tube. The micrococcal nuclease–digested chromatin fraction was precleared with 100 μl of blocked salmon sperm DNA/protein A agarose–50% slurry (Millipore, 16-157) at 4°C for 2 hours, and following centrifugation, the supernatant was transferred to fresh tubes. ChIP was carried out with anti-H3K4me3 (5 μg per reaction; ab8580, Abcam). After adding the antibody, the mixtures were incubated at 4°C overnight. To each reaction mixture, 20 μl of protein A agarose beads was added and incubated by rotating at 4°C for 1 hour. Beads were recovered by centrifugation and washed five times with low salt, high salt, LiCl, and TE buffer. Bound complex was eluted from the beads by incubating with 100 ml of elution buffer for twice at RT. Immunoeprecipitated DNA and input DNA were incubated with 5 μg of proteinase K (Invitrogen, 25530049) at 50°C for 1 hour and then purified by the QIAquick PCR Purification kit (Qiagen, 28104).

Purified DNA was used to construct sequencing libraries with 5 ng of DNA (ChIP or input). Libraries were prepared using the Rubicon ThruPLEX DNA-seq Library Prep Reagent Set for Illumina sequencing according to the manufacturer's recommendations. DNA quality was measured with an advanced analytical fragment analyzer with a high sensitivity chip. Fifty–base pair single-end reads per sample were obtained using the HiSeq 2500 platform from Illumina.

Bioinformatic analysis

RNA-seq tags reads were aligned to the mouse RefSeq mRNAs using TopHat2 with default parameters. Alignments with a mapping score < 10 were discarded using SAMtools. featureCounts was used to generate a matrix of mapped fragments per UCSC (University of California Santa Cruz) RefSeq known annotated gene, from which genes annotated by RefSeq as rRNA were discarded. Analysis for differential gene expression was performed using the edgeR package with the default setting. The differentially expressed genes between genotypes were defined with at least 1.2 FC and $P < 0.05$ (compared to WT). After drug treatment, the significantly reversed genes were defined with at least 1.2 FC and $P < 0.05$ (compared to saline). Genes with no known functions or very low counts (AveExp < 0) were excluded. GO analyses were generated using DAVID Functional Annotation Bioinformatics Microarray Analysis (*72*), as we previously described (*70*, *71*).

ChIPseq data (raw reads), in fastq format, were mapped with BWA (Burrows-Wheeler Aligner) against mouse reference genome (GRCm38/mm10) with the default setting for single-end fastq format. Peak calling was performed using MACS2 package in R with set extension size of 140 base pairs. In MACS2 package, the detection window slides across the genome to find enriched regions, which have twofold (default) more reads than background. MACS2 calculates the *P* value for each peak using a dynamic Poisson distribution. False discovery rate (FDR) values are calculated using the Benjamini-Hochberg correction. Peak calling cutoff was set at the minimal *P* value of 0.01 or FDR of 0.05. All graphs were generated using the IGV (Integrative Genomics Viewer) software.

To generate the circos plots, differentially expressed genomic data with significantly increased mRNA (RNA-seq) or H3K4me3 occupancy (ChIPseq) in P301S Tau mice were assigned to the *Mus musculus* mm10 genome, which contains all chromosomes except for sex chromosomes (20 and 21). The circos plot was designed as follows: (i) A scatter plot was applied to the most outer layer representing the log(*P*) values for each differential gene on each chromosome; the further out the dot (data point) is, the more significant the differential gene is. (ii) The second layer is the chromosome number (1 to 19) from the mm10 genome. (iii) The third layer is the log(FC) of each differential gene, represented as an area plot. (iv) The next layer is the top-ranking gene (by *P* value) on each chromosome. (v) The most inner layer is a rectangular plot representing the position of each data point on the chromosome. AMP-AD data were obtained from Agora, a platform initially developed by the National Institute on Aging–funded AMP-AD consortium that shares evidence in support of AD target discovery.

Statistical analysis

Data were analyzed with GraphPad Prism v.6 (GraphPad), Clampfit (Molecular Devices, Sunnyvale, CA), and KaleidaGraph (Synergy Software, Reading, PA). All values are means ± SEM. Differences between two groups were assessed with paired or unpaired Student's *t* test. Differences between more than two groups were assessed with one-way or two-way ANOVA, followed by post hoc Bonferroni tests for multiple comparisons.

SUPPLEMENTARY MATERIALS

Supplementary material for this article is available at http://advances.sciencemag.org/cgi/content/full/6/50/eabc8096/DC1

View/request a protocol for this paper from *Bio-protocol*.

REFERENCES AND NOTES

1. C. Ballatore, V. M. Lee, J. Q. Trojanowski, Tau-mediated neurodegeneration in Alzheimer's disease and related disorders. *Nat. Rev. Neurosci.* **8**, 663–672 (2007).
2. E. E. Congdon, E. M. Sigurdsson, Tau-targeting therapies for Alzheimer disease. *Nat. Rev. Neurol.* **14**, 399–415 (2018).
3. T. E. Tracy, L. Gan, Tau-mediated synaptic and neuronal dysfunction in neurodegenerative disease. *Curr. Opin. Neurobiol.* **51**, 134–138 (2018).
4. M. F. Mehler, Epigenetic principles and mechanisms underlying nervous system functions in health and disease. *Prog. Neurobiol.* **86**, 305–341 (2008).
5. R. Lardenoije, A. Iatrou, G. Kenis, K. Kompotis, H. W. M. Steinbusch, D. Mastroeni, P. Coleman, C. A. Lemere, P. R. Hof, D. L. A. van den Hove, B. P. F. Rutten, The epigenetics of aging and neurodegeneration. *Prog. Neurobiol.* **131**, 21–64 (2015).
6. D. M. Chuang, Y. Leng, Z. Marinova, H. J. Kim, C. T. Chiu, Multiple roles of HDAC inhibition in neurodegenerative conditions. *Trends Neurosci.* **32**, 591–601 (2009).
7. A. Berson, R. Nativio, S. L. Berger, N. M. Bonini, Epigenetic regulation in neurodegenerative diseases. *Trends Neurosci.* **41**, 587–598 (2018).
8. S. Parkel, J. P. Lopez-Atalaya, A. Barco, Histone H3 lysine methylation in cognition and intellectual disability disorders. *Learn. Mem.* **20**, 570–579 (2013).
9. T. J. Jarome, F. D. Lubin, Histone lysine methylation: Critical regulator of memory and behavior. *Rev. Neurosci.* **24**, 375–387 (2013).
10. E. Shen, H. Shulha, Z. Weng, S. Akbarian, Regulation of histone H3K4 methylation in brain development and disease. *Philos. Trans. R. Soc. Lond. B Biol. Sci.* **369**, 20130514 (2014).
11. W. D. Jones, D. Dafou, M. McEntagart, W. J. Woollard, F. V. Elmslie, M. Holder-Espinasse, M. Irving, A. K. Saggar, S. Smithson, R. C. Trembath, C. Deshpande, M. A. Simpson, De novo mutations in MLL cause Wiedemann-Steiner syndrome. *Am. J. Hum. Genet.* **91**, 358–364 (2012).
12. S. B. Ng, A. W. Bigham, K. J. Buckingham, M. C. Hannibal, M. J. McMillin, H. I. Gildersleeve, A. E. Beck, H. K. Tabor, G. M. Cooper, H. C. Mefford, C. Lee, E. H. Turner, J. D. Smith, M. J. Rieder, K. I. Yoshiura, N. Matsumoto, T. Ohta, N. Niikawa, D. A. Nickerson, M. J. Bamshad, J. Shendure, Exome sequencing identifies MLL2 mutations as a cause of Kabuki syndrome. *Nat. Genet.* **42**, 790–793 (2010).
13. L. R. Jensen, M. Amende, U. Gurok, B. Moser, V. Gimmel, A. Tzschach, A. R. Janecke, G. Tariverdian, J. Chelly, J. P. Fryns, H. van Esch, T. Kleefstra, B. Hamel, C. Moraine, J. Gécz, G. Turner, R. Reinhardt, V. M. Kalscheuer, H. H. Ropers, S. Lenzner, Mutations in the JARID1C gene, which is involved in transcriptional regulation and chromatin remodeling, cause X-linked mental retardation. *Am. J. Hum. Genet.* **76**, 227–236 (2005).
14. I. Iossifov, B. J. O'Roak, S. J. Sanders, M. Ronemus, N. Krumm, D. Levy, H. A. Stessman, K. T. Witherspoon, L. Vives, K. E. Patterson, J. D. Smith, B. Paeper, D. A. Nickerson, J. Dea, S. Dong, L. E. Gonzalez, J. D. Mandell, S. M. Mane, M. T. Murtha, C. A. Sullivan, M. F. Walker, Z. Waqar, L. Wei, A. J. Willsey, B. Yamrom, Y.-h. Lee, E. Grabowska, E. Dalkic, Z. Wang, S. Marks, P. Andrews, A. Leotta, J. Kendall, I. Hakker, J. Rosenbaum, B. Ma, L. Rodgers, J. Troge, G. Narzisi, S. Yoon, M. C. Schatz, K. Ye, W. R. M. Combie, J. Shendure, E. E. Eichler, M. W. State, M. Wigler, The contribution of de novo coding mutations to autism spectrum disorder. *Nature* **515**, 216–221 (2014).
15. H. Santos-Rosa, R. Schneider, A. J. Bannister, J. Sherriff, B. E. Bernstein, N. C. T. Emre, S. L. Schreiber, J. Mellor, T. Kouzarides, Active genes are tri-methylated at K4 of histone H3. *Nature* **419**, 407–411 (2002).
16. P. S. Goldman-Rakic, Cellular basis of working memory. *Neuron* **14**, 477–485 (1995).
17. G. E. Garrido, S. S. Furuie, C. A. Buchpiguel, C. M. C. Bottino, O. P. Almeida, C. G. Cid, C. H. P. Camargo, C. C. Castro, M. F. Glabus, G. F. Busatto, Relation between medial temporal atrophy and functional brain activity during memory processing in Alzheimer's disease: A combined MRI and SPECT study. *J. Neurol. Neurosurg. Psychiatry* **73**, 508–516 (2002).
18. F. Remy, F. Mirrashed, B. Campbell, W. Richter, Verbal episodic memory impairment in Alzheimer's disease: A combined structural and functional MRI study. *Neuroimage* **25**, 253–266 (2005).
19. D. Maillet, M. N. Rajah, Association between prefrontal activity and volume change in prefrontal and medial temporal lobes in aging and dementia: A review. *Ageing Res. Rev.* **12**, 479–489 (2013).
20. B. Allen, E. Ingram, M. Takao, M. J. Smith, R. Jakes, K. Virdee, H. Yoshida, M. Holzer, M. Craxton, P. C. Emson, C. Atzori, A. Migheli, R. A. Crowther, B. Ghetti, M. G. Spillantini, M. Goedert, Abundant tau filaments and nonapoptotic neurodegeneration in transgenic mice expressing human P301S tau protein. *J. Neurosci.* **22**, 9340–9351 (2002).
21. Y. Shi, K. Yamada, S. A. Liddelow, S. T. Smith, L. Zhao, W. Luo, R. M. Tsai, S. Spina, L. T. Grinberg, J. C. Rojas, G. Gallardo, K. Wang, J. Roh, G. Robinson, M. B. Finn, H. Jiang, P. M. Sullivan, C. Baufeld, M. W. Wood, C. Sutphen, L. M. Cue, C. Xiong, J. L. Del-Aguila, J. C. Morris, C. Cruchaga; Alzheimer's Disease Neuroimaging Initiative, A. M. Fagan, B. L. Miller, A. L. Boxer, W. W. Seeley, O. Butovsky, B. A. Barres, S. M. Paul, D. M. Holtzman, ApoE4 markedly exacerbates tau-mediated neurodegeneration in a mouse model of tauopathy. *Nature* **549**, 523–527 (2017).
22. Y. Yoshiyama, M. Higuchi, B. Zhang, S. M. Huang, N. Iwata, T. C. Saido, J. Maeda, T. Suhara, J. Q. Trojanowski, V. M. Y. Lee, Synapse loss and microglial activation precede tangles in a P301S tauopathy mouse model. *Neuron* **53**, 337–351 (2007).
23. S. W. Min, S. H. Cho, Y. Zhou, S. Schroeder, V. Haroutunian, W. W. Seeley, E. J. Huang, Y. Shen, E. Masliah, C. Mukherjee, D. Meyers, P. A. Cole, M. Ott, L. Gan, Acetylation of tau inhibits its degradation and contributes to tauopathy. *Neuron* **67**, 953–966 (2010).
24. Y. Li, J. Han, Y. Zhang, F. Cao, Z. Liu, S. Li, J. Wu, C. Hu, Y. Wang, J. Shuai, J. Chen, L. Cao, D. Li, P. Shi, C. Tian, J. Zhang, Y. Dou, G. Li, Y. Chen, M. Lei, Structural basis for activity regulation of MLL family methyltransferases. *Nature* **530**, 447–452 (2016).
25. G. Senisterra, H. Wu, A. Allali-Hassani, G. A. Wasney, D. Barsyte-Lovejoy, L. Dombrovski, A. Dong, K. T. Nguyen, D. Smil, Y. Bolshan, T. Hajian, H. He, A. Seitova, I. Chau, F. Li, G. Poda, J. F. Couture, P. J. Brown, R. al-Awar, M. Schapira, C. H. Arrowsmith, M. Vedadi, Small-molecule inhibition of MLL activity by disruption of its interaction with WDR5. *Biochem. J.* **449**, 151–159 (2013).
26. R. C. Rao, Y. Dou, Hijacked in cancer: The KMT2 (MLL) family of methyltransferases. *Nat. Rev. Cancer* **15**, 334–346 (2015).
27. H. Oakley, S. L. Cole, S. Logan, E. Maus, P. Shao, J. Craft, A. Guillozet-Bongaarts, M. Ohno, J. Disterhoft, L. van Eldik, R. Berry, R. Vassar, Intraneuronal β-amyloid aggregates, neurodegeneration, and neuron loss in transgenic mice with five familial Alzheimer's disease mutations: Potential factors in amyloid plaque formation. *J. Neurosci.* **26**, 10129–10140 (2006).
28. C. Haass, D. J. Selkoe, Soluble protein oligomers in neurodegeneration: Lessons from the Alzheimer's amyloid beta-peptide. *Nat. Rev. Mol. Cell Biol.* **8**, 101–112 (2007).
29. G. M. Shankar, S. Li, T. H. Mehta, A. Garcia-Munoz, N. E. Shepardson, I. Smith, F. M. Brett, M. A. Farrell, M. J. Rowan, C. A. Lemere, C. M. Regan, D. M. Walsh, B. L. Sabatini, D. J. Selkoe, Amyloid-β protein dimers isolated directly from Alzheimer's brains impair synaptic plasticity and memory. *Nat. Med.* **14**, 837–842 (2008).
30. Y. Zheng, A. Liu, Z. J. Wang, Q. Cao, W. Wang, L. Lin, K. Ma, F. Zhang, J. Wei, E. Matas, J. Cheng, G. J. Chen, X. Wang, Z. Yan, Inhibition of EHMT1/2 rescues synaptic and cognitive functions for Alzheimer's disease. *Brain* **142**, 787–807 (2019).
31. P. S. Pinheiro, C. Mulle, Presynaptic glutamate receptors: Physiological functions and mechanisms of action. *Nat. Rev. Neurosci.* **9**, 423–436 (2008).
32. P. T. Francis, Glutamatergic systems in Alzheimer's disease. *Int. J. Geriatr. Psychiatry* **18**, S15–S21 (2003).
33. E. H. Chang, M. J. Savage, D. G. Flood, J. M. Thomas, R. B. Levy, V. Mahadomrongkul, T. Shirao, C. Aoki, P. T. Huerta, AMPA receptor downscaling at the onset of Alzheimer's disease pathology in double knockin mice. *Proc. Natl. Acad. Sci. U.S.A.* **103**, 3410–3415 (2006).
34. L. Lin, A. Liu, H. Li, J. Feng, Z. Yan, Inhibition of histone methyltransferases EHMT1/2 reverses amyloid-β-induced loss of AMPAR currents in human stem cell-derived cortical neurons. *J. Alzheimers Dis.* **70**, 1175–1185 (2019).
35. F. Lang, C. Böhmer, M. Palmada, G. Seebohm, N. Strutz-Seebohm, V. Vallon, (Patho) physiological significance of the serum- and glucocorticoid-inducible kinase isoforms. *Physiol. Rev.* **86**, 1151–1178 (2006).
36. B. Schoenebeck, V. Bader, X. R. Zhu, B. Schmitz, H. Lübbert, C. C. Stichel, Sgk1, a cell survival response in neurodegenerative diseases. *Mol. Cell. Neurosci.* **30**, 249–264 (2005).
37. J. Chun, T. Kwon, E. J. Lee, C. H. Kim, Y. S. Han, S. K. Hong, S. Hyun, S. S. Kang, 14-3-3 Protein mediates phosphorylation of microtubule-associated protein tau by serum- and glucocorticoid-induced protein kinase 1. *Mol. Cells* **18**, 360–368 (2004).
38. C. X. Gong, K. Iqbal, Hyperphosphorylation of microtubule-associated protein tau: A promising therapeutic target for Alzheimer disease. *Curr. Med. Chem.* **15**, 2321–2328 (2008).
39. B. Dubois, H. H. Feldman, C. Jacova, H. Hampel, J. L. Molinuevo, K. Blennow, S. T. DeKosky, S. Gauthier, D. Selkoe, R. Bateman, S. Cappa, S. Crutch, S. Engelborghs, G. B. Frisoni, N. C. Fox, D. Galasko, M. O. Habert, G. A. Jicha, A. Nordberg, F. Pasquier, G. Rabinovici, P. Robert, C. Rowe, S. Salloway, M. Sarazin, S. Epelbaum, L. C. de Souza, B. Vellas, P. J. Visser, L. Schneider, Y. Stern, P. Scheltens, J. L. Cummings, Advancing research diagnostic criteria for Alzheimer's disease: The IWG-2 criteria. *Lancet Neurol.* **13**, 614–629 (2014).
40. Y. C. Yang, C. H. Lin, E. H. Lee, Serum- and glucocorticoid-inducible kinase 1 (SGK1) increases neurite formation through microtubule depolymerization by SGK1 and by SGK1 phosphorylation of tau. *Mol. Cell. Biol.* **26**, 8357–8370 (2006).
41. J. Z. Wang, Y. Y. Xia, I. Grundke-Iqbal, K. Iqbal, Abnormal hyperphosphorylation of tau: Sites, regulation, and molecular mechanism of neurofibrillary degeneration. *J. Alzheimers Dis.* **33** (Suppl. 1), S123–S139 (2013).
42. A. B. Sherk, D. E. Frigo, C. G. Schnackenberg, J. D. Bray, N. J. Laping, W. Trizna, M. Hammond, J. R. Patterson, S. K. Thompson, D. Kazmin, J. D. Norris, D. P. McDonnell, Development of a small-molecule serum- and glucocorticoid-regulated kinase-1

antagonist and its evaluation as a prostate cancer therapeutic. *Cancer Res.* **68**, 7475–7483 (2008).
43. E. Suberbielle, B. Djukic, M. Evans, D. H. Kim, P. Taneja, X. Wang, M. Finucane, J. Knox, K. Ho, N. Devidze, E. Masliah, L. Mucke, DNA repair factor BRCA1 depletion occurs in Alzheimer brains and impairs cognitive function in mice. *Nat. Commun.* **6**, 8897 (2015).
44. F. L. Heppner, R. M. Ransohoff, B. Becher, Immune attack: The role of inflammation in Alzheimer disease. *Nat. Rev. Neurosci.* **16**, 358–372 (2015).
45. C. Cadonic, M. G. Sabbir, B. C. Albensi, Mechanisms of mitochondrial dysfunction in Alzheimer's disease. *Mol. Neurobiol.* **53**, 6078–6090 (2016).
46. V. Sorrentino, M. Romani, L. Mouchiroud, J. S. Beck, H. Zhang, D. D'Amico, N. Moullan, F. Potenza, A. W. Schmid, S. Rietsch, S. E. Counts, J. Auwerx, Enhancing mitochondrial proteostasis reduces amyloid-β proteotoxicity. *Nature* **552**, 187–193 (2017).
47. V. Boccardi, L. Pelini, S. Ercolani, C. Ruggiero, P. Mecocci, From cellular senescence to Alzheimer's disease: The role of telomere shortening. *Ageing Res. Rev.* **22**, 1–8 (2015).
48. L. Gan, M. R. Cookson, L. Petrucelli, A. R. La Spada, Converging pathways in neurodegeneration, from genetics to mechanisms. *Nat. Neurosci.* **21**, 1300–1309 (2018).
49. J. Graff, D. Kim, M. M. Dobbin, L. H. Tsai, Epigenetic regulation of gene expression in physiological and pathological brain processes. *Physiol. Rev.* **91**, 603–649 (2011).
50. E. L. Greer, T. J. Maures, A. G. Hauswirth, E. M. Green, D. S. Leeman, G. S. Maro, S. Han, M. R. Banko, O. Gozani, A. Brunet, Members of the H3K4 trimethylation complex regulate lifespan in a germline-dependent manner in *C. elegans*. *Nature* **466**, 383–387 (2010).
51. H. Mathys, J. Davila-Velderrain, Z. Peng, F. Gao, S. Mohammadi, J. Z. Young, M. Menon, L. He, F. Abdurrob, X. Jiang, A. J. Martorell, R. M. Ransohoff, B. P. Hafler, D. A. Bennett, M. Kellis, L. H. Tsai, Single-cell transcriptomic analysis of Alzheimer's disease. *Nature* **570**, 332–337 (2019).
52. T. Wu, B. Dejanovic, V. D. Gandham, A. Gogineni, R. Edmonds, S. Schauer, K. Srinivasan, M. A. Huntley, Y. Wang, T. M. Wang, M. Hedehus, K. H. Barck, M. Stark, H. Ngu, O. Foreman, W. J. Meilandt, J. Elstrott, M. C. Chang, D. V. Hansen, R. A. D. Carano, M. Sheng, J. E. Hanson, Complement C3 is activated in human AD brain and is required for neurodegeneration in mouse models of amyloidosis and tauopathy. *Cell Rep.* **28**, 2111–2123.e6 (2019).
53. Y. Zhou, W. M. Song, P. S. Andhey, A. Swain, T. Levy, K. R. Miller, P. L. Poliani, M. Cominelli, S. Grover, S. Gilfillan, M. Cella, T. K. Ulland, K. Zaitsev, A. Miyashita, T. Ikeuchi, M. Sainouchi, A. Kakita, D. A. Bennett, J. A. Schneider, M. R. Nichols, S. A. Beausoleil, J. D. Ulrich, D. M. Holtzman, M. N. Artyomov, M. Colonna, Human and mouse single-nucleus transcriptomics reveal TREM2-dependent and TREM2-independent cellular responses in Alzheimer's disease. *Nat. Med.* **26**, 131–142 (2020).
54. M. Obulesu, M. J. Lakshmi, Apoptosis in Alzheimer's disease: An understanding of the physiology, pathology and therapeutic avenues. *Neurochem. Res.* **39**, 2301–2312 (2014).
55. M. P. Mattson, Apoptosis in neurodegenerative disorders. *Nat. Rev. Mol. Cell Biol.* **1**, 120–130 (2000).
56. R. Madabhushi, L. Pan, L. H. Tsai, DNA damage and its links to neurodegeneration. *Neuron* **83**, 266–282 (2014).
57. J. R. Bamburg, G. S. Bloom, Cytoskeletal pathologies of Alzheimer disease. *Cell Motil. Cytoskeleton* **66**, 635–649 (2009).
58. P. Sahin, C. McCaig, J. Jeevahan, J. T. Murray, A. H. Hainsworth, The cell survival kinase SGK1 and its targets FOXO3a and NDRG1 in aged human brain. *Neuropathol. Appl. Neurobiol.* **39**, 623–633 (2013).
59. R. Koldamova, J. Schug, M. Lefterova, A. A. Cronican, N. F. Fitz, F. A. Davenport, A. Carter, E. L. Castranio, I. Lefterov, Genome-wide approaches reveal EGR1-controlled regulatory networks associated with neurodegeneration. *Neurobiol. Dis.* **63**, 107–114 (2014).
60. C. C. Shieh, M. Coghlan, J. P. Sullivan, M. Gopalakrishnan, Potassium channels: Molecular defects, diseases, and therapeutic opportunities. *Pharmacol. Rev.* **52**, 557–594 (2000).
61. M. Canal, J. Romani-Aumedes, N. Martin-Flores, V. Perez-Fernandez, C. Malagelada, RTP801/REDD1: A stress coping regulator that turns into a troublemaker in neurodegenerative disorders. *Front. Cell. Neurosci.* **8**, 313 (2014).
62. J. L. Kwapis, Y. Alaghband, E. A. Kramár, A. J. López, A. Vogel Ciernia, A. O. White, G. Shu, D. Rhee, C. M. Michael, E. Montellier, Y. Liu, C. N. Magnan, S. Chen, P. Sassone-Corsi, P. Baldi, D. P. Matheos, M. A. Wood, Epigenetic regulation of the circadian gene *Per1* contributes to age-related changes in hippocampal memory. *Nat. Commun.* **9**, 3323 (2018).
63. M. P. Mattson, C. Culmsee, Z. Yu, S. Camandola, Roles of nuclear factor κB in neuronal survival and plasticity. *J. Neurochem.* **74**, 443–456 (2000).
64. E. Gjoneska, A. R. Pfenning, H. Mathys, G. Quon, A. Kundaje, L.-H. Tsai, M. Kellis, Conserved epigenomic signals in mice and humans reveal immune basis of Alzheimer's disease. *Nature* **518**, 365–369 (2015).
65. B. Bai, X. Wang, Y. Li, P. C. Chen, K. Yu, K. K. Dey, J. M. Yarbro, X. Han, B. M. Lutz, S. Rao, Y. Jiao, J. M. Sifford, J. Han, M. Wang, H. Tan, T. I. Shaw, J. H. Cho, S. Zhou, H. Wang, M. Niu, A. Mancieri, K. A. Messler, X. Sun, Z. Wu, V. Pagala, A. A. High, W. Bi, H. Zhang, H. Chi, V. Haroutunian, B. Zhang, T. G. Beach, G. Yu, J. Peng, Deep multilayer brain proteomics identifies molecular networks in Alzheimer's disease progression. *Neuron* **105**, 975–991.e7 (2020).
66. L. J. Duffney, P. Zhong, J. Wei, E. Matas, J. Cheng, L. Qin, K. Ma, D. M. Dietz, Y. Kajiwara, J. D. Buxbaum, Z. Yan, Autism-like deficits in *Shank3*-deficient mice are rescued by targeting actin regulators. *Cell Rep.* **11**, 1400–1413 (2015).
67. L. Qin, K. Ma, Z. J. Wang, Z. Hu, E. Matas, J. Wei, Z. Yan, Social deficits in Shank3-deficient mouse models of autism are rescued by histone deacetylase (HDAC) inhibition. *Nat. Neurosci.* **21**, 564–575 (2018).
68. E. Y. Yuen, J. Wei, W. Liu, P. Zhong, X. Li, Z. Yan, Repeated stress causes cognitive impairment by suppressing glutamate receptor expression and function in prefrontal cortex. *Neuron* **73**, 962–977 (2012).
69. C. S. Rosenfeld, S. A. Ferguson, Barnes maze testing strategies with small and large rodent models. *J. Vis. Exp.*, e51194 (2014).
70. M. Rapanelli, T. Tan, W. Wang, X. Wang, Z. J. Wang, P. Zhong, L. Frick, L. Qin, K. Ma, J. Qu, Z. Yan, Behavioral, circuitry, and molecular aberrations by region-specific deficiency of the high-risk autism gene *Cul3*. *Mol. Psychiatry* , (2019).
71. Z. J. Wang, P. Zhong, K. Ma, J.-S. Seo, F. Yang, Z. Hu, F. Zhang, L. Lin, J. Wang, T. Liu, E. Matas, P. Greengard, Z. Yan, Amelioration of autism-like social deficits by targeting histone methyltransferases EHMT1/2 in *Shank3*-deficient mice. *Mol. Psychiatry* **25**, 2517–2533 (2020).
72. D. W. Huang, B. T. Sherman, R. A. Lempicki, Systematic and integrative analysis of large gene lists using DAVID bioinformatics resources. *Nat. Protoc.* **4**, 44–57 (2009).

Acknowledgments: We thank X. Chen and B. Rein for excellent technical support. We acknowledge the support of University at Buffalo's Genomics and Bioinformatics Core and the New York State Center of Excellence in Bioinformatics and Life Sciences. We also thank NIH NeuroBioBank for providing postmortem brain tissues from patients with AD and control subjects. **Funding:** This work was supported by grants from the NIH (AG064656, AG056060, and AG067597) to Z.Y. **Author contributions:** Q.C. performed behavioral, biochemical, immunohistochemical, and molecular biological experiments, parts of bioinformatic analysis, analyzed data, and wrote the draft. W.W. performed electrophysiological experiments and analyzed data. J.B.W. and F.Y. analyzed genomic data. J.B.W. also performed some behavioral tests. Z.-J. W. prepared samples for ChIPseq. Z.Y. designed experiments, supervised the project, and wrote the paper. **Competing interests:** The authors declare that they have no competing interests. **Data and materials availability:** All data needed to evaluate the conclusions in the paper are present in the paper and/or the Supplementary Materials. Additional data related to this paper may be requested from the authors. Genomic data are deposited in a public repository. The access number and the dataset are available for access.

Submitted 14 May 2020
Accepted 23 October 2020
Published 9 December 2020
10.1126/sciadv.abc8096

Citation: Q. Cao, W. Wang, J. B. Williams, F. Yang, Z.-J. Wang, Z. Yan, Targeting histone K4 trimethylation for treatment of cognitive and synaptic deficits in mouse models of Alzheimer's disease. *Sci. Adv.* **6**, eabc8096 (2020).

Science Advances

Targeting histone K4 trimethylation for treatment of cognitive and synaptic deficits in mouse models of Alzheimer's disease

Qing Cao, Wei Wang, Jamal B. Williams, Fengwei Yang, Zi-Jun Wang and Zhen Yan

Sci Adv **6** (50), eabc8096.
DOI: 10.1126/sciadv.abc8096

Science Advances (ISSN 2375-2548) is published by the American Association for the Advancement of Science, 1200 New York Avenue NW, Washington, DC 20005. The title *Science Advances* is a registered trademark of AAAS.